AN INVESTIGATION INTO THE NONINVASIVE
ASSESSMENT OF BONE DENSITY USING
MULTIPLEXED COMPTON SCATTERED
TOMOGRAPHY

THESIS

Marc J. Sands, Captain, USAF
AFIT/GAP/ENP/99M-10

19990402 011

DEPARTMENT OF THE AIR FORCE
AIR UNIVERSITY
AIR FORCE INSTITUTE OF TECHNOLOGY

Wright-Patterson Air Force Base, Ohio

AN INVESTIGATION INTO THE NONINVASIVE ASSESSMENT OF BONE

DENSITY USING MULTIPLEXED COMPTON SCATTERED TOMOGRAPHY

THESIS

Presented to the Faculty of the School of Engineering

of the Air Force Institute of Technology

Air University

In Partial Fulfillment of the Requirements for the Degree of

Master of Science in Nuclear Engineering

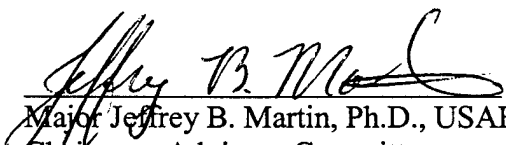Marc J. Sands, B.S.

Captain, USAF

March 1999

AN INVESTIGATION INTO THE NONINVASIVE ASSESSMENT OF BONE

DENSITY USING MULTIPLEXED COMPTON SCATTERED TOMOGRAPHY

Marc J. Sands, B.S.

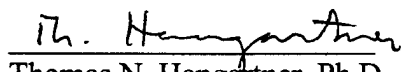Captain, USAF

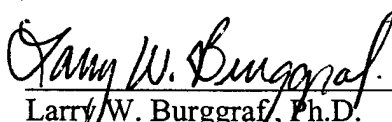Approved: Date:

Major Jeffrey B. Martin, Ph.D., USAF
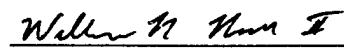Chairman, Advisory Committee

8 Mar '99

Thomas N. Hangartner, Ph.D.
Member, Advisory Committee

8 March 99

Larry W. Burggraf, Ph.D.
Member, Advisory Committee

8 Mar 99

Major William R. Ruck, USAF
Member, Advisory Committee

6 MAR 99

Acknowledgment

I am grateful to my thesis advisor Dr. Jeffrey Martin for his outstanding help and guidance in this project. I am also grateful to the members of my advisory committee, Dr. Thomas Hangartner, Dr. Larry Burggraf and Mr. William Ruck for their additional input and extremely helpful advice.

I want to thank Mr. Russ Hastings, Mr. Condie Inman, and Mr. Jan LeValley of the AFIT machine shop for their expert craftsmanship and mechanical support in the development of my equipment. They made scratch drawings into reality and did so flawlessly.

I would like to thank Lt. Dennis Rand and Capt. Scott Nemmers for their fantastic editing and constructive comments, as well as Ms. Diana K. Jordan for her format specialty.

I especially want to thank my family. Bob, Tye and Scott – thank you for your support and encouragement during this time.

Most of all, I need to thank my wife. Angela – you have provided unwavering support and complete understanding throughout this degree program. I could not have done this without you. Thank you.

Table of Contents

List of Figures

List of Tables

AFIT/GAP/ENP/99M-10

Abstract

The purpose of this research is to investigate the application of a Compton scatter imaging technique to measure bone density. A demonstration Multiplexed Compton Scatter Tomograph (MCST) was assembled to demonstrate the feasibility of detecting osteoporosis by modifying a system originally designed to detect hidden corrosion in aluminum aircraft wings. Measurements were performed on an aluminum phantom representing a wrist bone containing varying densities in the center and varying thickness of the cortical shell. The densities in the center are comparable to normal trabecular bone, sixty-percent of normal trabecular bone and a void. The MCST images of the phantom were then compared to simulated images from a detector. The images and simulations were also compared to images from a clinical computed tomography (CT) scanner. Based on the results, the MCST can discern the features represented by the trabecular bone. The system was able to differentiate normal, osteoporotic and void densities.

AN INVESTIGATION INTO THE NONINVASIVE ASSESSMENT OF BONE DENSITY USING MULTIPLEXED COMPTON SCATTERED TOMOGRAPHY

I. INTRODUCTION

Motivation

Osteoporosis afflicts approximately 28 million people in the United States, with an estimated cost of $38 million per day [NOF, 1997]. Osteoporosis is a serious medical condition characterized by severe weakening of the skeletal structure and often goes unnoticed. Accurate noninvasive measurements and characterization of the bone density are required in order to detect osteoporosis in a patient. Over the last decade, medical systems have matured in the area of bone mass measurements. Current clinical systems use attenuation of photons to calculate the densities in bone. However, in materials that have low atomic numbers and at the gamma-ray energies of interest for bone imaging, 30 - 100 keV, the dominant photon interaction mechanism is scattering, not absorption [Cho, 1993]. A Multiplexed Compton Scatter Tomograph (MCST), funded by the U.S. Air Force to detect corrosion in aging aluminum aircraft skin, detects scattered photons from a sample which are used to produce a two-dimensional image of the sample's electron density. This system has been modified to image bone density. By using this system, we will attempt to determine the feasibility of the MCST to detect osteoporosis.

The feasibility of using Compton scattering in a clinical environment to characterize bone density loss can be investigated using the ability of the MCST to measure changes in trabecular bone density. The information gained from the MCST results could be used for the development of a more robust detection system.

<u>Description of Osteoporosis</u>

Osteoporosis, literally "porous bone", is characterized by a severe decrease in bone density, thereby increasing the fragility of the patient's bone [Narhi, 1998]. The thinning and subsequent weakening of the bone structure leads to increased risk of fracturing the bones. Long bones are made of a cylindrical exterior region, the cortical bone and towards both ends of an inner less dense region, the trabecular bone. The cortical bone maintains a thickness of approximately 2.5 to 3.5 mm in the midshaft of the arm and leg bones until about 30-50 years of age, after which the thickness slowly decays [Hangartner and Gilsanz, 1996]. The most significant group afflicted where this condition can lead to fractures in women who have reached menopause.

The reduction of trabecular bone density in the years just before menopause is approximately 0.5-1 % per year; however, in the first several years after menopause, the bone loss rate increases to 2-3% per year. Therefore, the reduction slows to a rate of about 1% per year [Heilmann, et. al., 1997]. The decline in this regeneration process is the focus of clinical investigations to identify patients in early stages of osteoporosis [Tortora, 1987].

Figure 1-1 shows the difference in the bone structure from a normal bone to that of an osteoporotic bone. This makes the mapping of the bone density in a patient critical to determining the extent of progression of the condition [NOF, 1998].
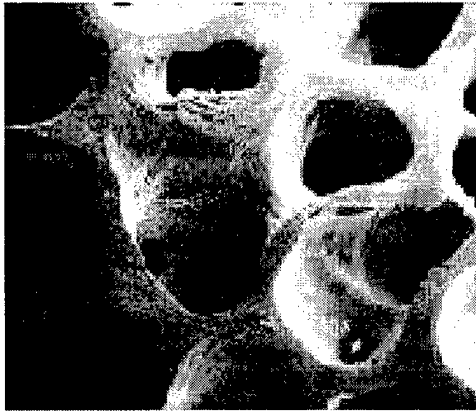
Figure 1-1. These images show weakening effects of osteoporosis on bone. (a) Image of trabecular bone structure in a normal patient. (b) Image of trabecular bone structure of a patient with osteoporosis.

The positive identification of osteoporosis in its early stages can significantly increase the effectiveness of the medical community to counter its effect. The patient can halt the deterioration process significantly with medications and weight bearing exercises to reduce bone loss. Advances in the detection systems have also allowed precise characterization of the status of the condition. Technical advancements have led to the capability to accurately detect relatively small changes in bone density over time for a particular patient [Hangartner, 1998]. A high degree of precision is requisite when a small percentage of bone loss indicates the presence of osteoporosis. For people over 40 years old, an annual loss of 1 percent of bone density is considered standard, whereas greater than 2 percent is seen as excessive [Barzel, 1978].

Current clinical systems are usually either computed tomography (CT), or dual energy x-ray absorptiometry (DXA) systems. A common CT scanner uses a source on one side of the object scanned, with a row of detectors on the opposite side. Calculations of the fraction of emitted photons that pass through the material to the detector provide a

3

measure of the density of the material between the two. Reconstruction of a CT image requires knowledge of the exact relative position of the detector and source, and proper characterization of the detection system. The information collected is a line integral of the attenuation coefficient from the source to each detector.

The transmitted photons represent the fraction of incident radiation not absorbed by the body. The logarithm of this ratio represents the summation of the attenuation coefficients along the line path of the photons. This integral is a function of the tissue residing along the line from the source to detector. A full set of line integrals from a given source position is called a projection. The complete data set necessary for reconstruction rotating the source-detector assembly around the sample and collecting projections over at least 180 degrees. The distribution of the attenuation coefficients is then determined by using one of several image reconstruction techniques. Figure 1-2 shows an illustrative design of a single position in CT geometry.

The benefits of these methods are good spatial resolution and sensitivity to relative changes in the trabecular bone. This manner of obtaining the linear attenuation coefficients does not allow for direct measurement of information concerning the electron densities of the sample. The benefit of using Compton scattering is its linear dependence on the atomic number, Z, over a large range of energies from the low keV into the MeV range. By using the Compton scattering, information is gained on the electron densities, and therefore the mass densities, of the imaged material [Arendtsz and Hussein, 1993].
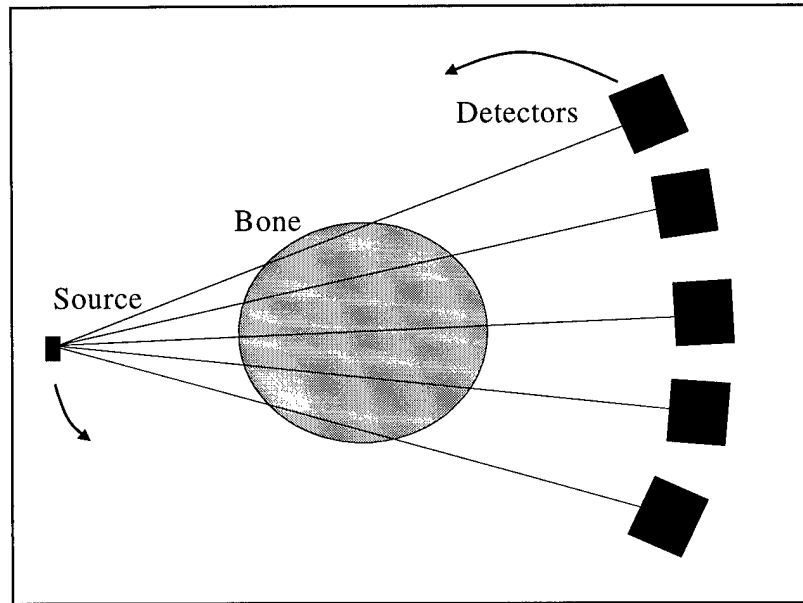
Figure 1-2. A typical CT configuration for bone density measurement. The source-detector assembly is rotated around the bone to construct overlapping line integrals.

The DXA system is very similar in regards to the physics and manner in which it measures the attenuation coefficients. DXA, however, uses two incident photon energies to calculate the attenuation coefficients of the bone and surrounding soft tissue [Lunar]. This method of differential photoabsorption also provides accurate detection and monitoring of osteoporotic bone. The major difference of the DXA is that it provides a projection image of the bone mass, not the bone density as in CT results.

The medical community predominately uses photoabsorption in their techniques of body tissue imaging. From transmission computed tomography to ordinary bone radiographs, the mechanism used is the ratio of transmitted to incident photons to create a visual image [Cho, 1993]. The energies typically used for medical applications are between 50 and 100 keV where the dominant photon interaction mechanism is Compton scatter and not absorption.

Compton scattering is also the dominant photon interaction mechanism in the bone at the energies of interest (88 keV). According to Garnet et al. (1973), incident photon energy of 100 keV is low enough to allow accurate measurements of bone using Compton scattering. It is possible to determine the angle of scatter simply by knowing initial and final energies of the photon by using the Compton scatter of a photon. An incident photon enters the material, scatters off an orbital electron, and exits the material. It is then detected by the system with a new energy of (E'). The governing equation (Equation 1-1) is a first order dependence of the scattered photon energy on its initial energy (E_0) and scattering angle θ.

$$E' = \frac{E_0}{1 + \frac{E_0}{m_0 c^2}(1 - \cos\theta)} \qquad (1\text{-}1)$$

where c is the speed of light, and m_0 is the rest mass of an electron.

Using a monoenergetic source, knowledge of the scatter origin can be determined from the scattered photon energy. Norton determined that the locus of points that make up the possible origins of scatter is an arc of a circle containing both the source and detector locations (Figure1-3). The radius of these "isogonic arcs" is a function of the scattered energy E' and thus the scattering angle θ [Norton, 1994]. With the scattered photon energies and knowledge of their scatter origin, a filtering reconstruction technique allows an image to be created.

When the composition of the sample material is constant, the probability of Compton scattering is proportional to the electron density of the sampled material. As

the mass density reduces, there is a linear decrease in the electron density in that region. With osteoporosis, this reduction of electron density can be monitored with a system that measures gamma rays Compton scattered from that object. Using the scattered photon energies and proper reconstruction techniques, an image of electron density is produced. This image of electron density has a linear relationship to the actual mass density. This method of imaging could lead to highly effective non-invasive inspection and monitoring of osteoporosis.

The validity of specific assumptions made with the Compton equation, in addition to other mechanisms involved in the data collection, are discussed in greater detail in Chapter II: Theory.
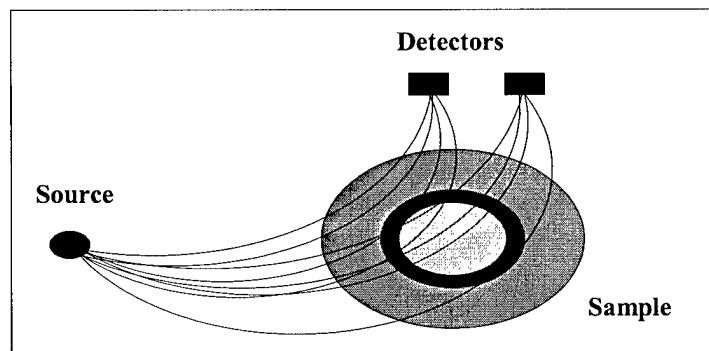
Figure 1-3. Isogonic arcs are the locus of points a scatter event could occur. The sample consists of a bone (black with gray core) surrounded by muscle tissue (dark gray). Here a mesh of isogonic lines through a sample determines the electron density of the bone.

Objective

The primary objective of this project is to investigate MCST as a potential method for monitoring osteoporosis. Evaluation of reconstructed bone phantom density images will determine the potential of the system to determine osteoporosis.

<u>General Approach</u>

The project included measuring three different trabecular bone width and two cortical bone densities in an aluminum phantom. The three values used in the trabecular bone are normal density, sixty percent of the normal density to simulate osteoporotic bone, and a void to demonstrate the extreme case. The osteoporotic simulation density is an extreme case and is not physically possible. The value was chosen to test the capability to discern an extreme density loss. The two cortical thicknesses had to demonstrate the effect of photon absorption by cortical bone on trabecular bone density determination.

A bone density phantom was to be fabricated under several restrictions. First, all of the materials needed to accurately model the proper electron density. Without the proper electron densities for each region, the results would not be meaningful for the intended medical application. Second, the materials needed to be homogeneous due to modeling and image reconstruction constraints. Third, the materials needed to be purchased at a reasonable cost. Finally, the design needed to incorporate limitations of the machines used to fabricate the phantom while maintaining a geometry that ensured reliable acquisition of data. All of these factors were taken into consideration during the design process to prevent compromising the relevance of the results. The phantom development is discussed in more detail in Chapter IV.

The MCST consists of five major components: detector array, gamma ray source, collimators, electronics and image reconstruction software. The source collimator was designed and utilized to provide a unique geometry in the original MCST. The collimator had to provide a uniform fan-beam of the source photons. This source

collimator was to be used with existing detector collimation, with the alignment of the source and detector collimators being critical to the data acquisition portion of the research.

The Scattergram code developed by Evans was to be used to characterize the region of interest where the phantom would be imaged. Single point sources were used to calculate the point responses as they varied within the region. These results would be placed into a polynomial fit to the Scattergram simulation code for implementation. The Scattergram would then be used to simulate each of the phantoms.

The data collection was to be done using the CAMAC (Computer Automated Measurement and Control) system to acquire the data, and commercial software would display the resulting spectra from the scattered photons.

The Scattergram code was expected to accurately calculate the output spectrum from the MCST detectors. The simulated spectra were to provide a comparison against which we could qualitatively measure the MCST data. This should benchmark the spectra and give an upper bound for the quality of the MCST images.

The image reconstruction algorithm was to create images from collected spectra. The images created from the simulated data were compared to the images created from the measured data.

<u>Sequence of Presentation</u>

Chapter II introduces the physics governing Compton scattering, the Klein-Nishina equation, Doppler broadening, and the effect of source fan-beam collimation on image quality. This chapter also describes the development done in Evans' Scattergram computational model and its importance in image reconstruction [Evans, *et al.*, 1997]. Chapter III describes the MCST components including detectors, electronics, collimation and software used. Chapter IV describes the complete procedures followed for the research. Chapter V reports the image comparison results. Chapter VI provides the research conclusions and recommendations for future work.

II. THEORY

This chapter describes the physics of the MCST process, including the Compton scattering from the sample and the corrections required to the Compton equation. This chapter also describes the deterministic computational code used to predict the energy spectrum from the sample and the image reconstruction algorithm used to map the energy data collected by the detector arrays into a spatial image.

Physics of Multiplexed Compton Scattered Tomography

Compton scattering. In 1923, Arthur H. Compton developed a scattering equation relating the initial and final energies of a photon to the angular deflection after an inelastic collision with an electron. For a given initial energy, this first-order equation describes a direct one-to-one correlation between the final photon energy and the scattering angle (Equation 1-1). Compton's equation assumes that the photon scatters off an unbound, at-rest electron. This assumption is not valid when dealing with bound orbital electrons; however, the Compton equation provides an excellent approximation and is widely used.

The Compton broadening invalidates the one-to-one relationship in the Compton equation between θ and E' in Equation 1-1 by causing some uncertainty in the determined angle, θ.

Compton broadening. Compton broadening, or Doppler broadening, arises when the incident photon scatters off a bound, moving electron. The additional momentum of the electron is evident in the dispersion of the energy spectrum from monoenergetic

11

photons being scattered through a constant angle [Ordonez, *et al.*, 1997], shown in Figure 2-1.
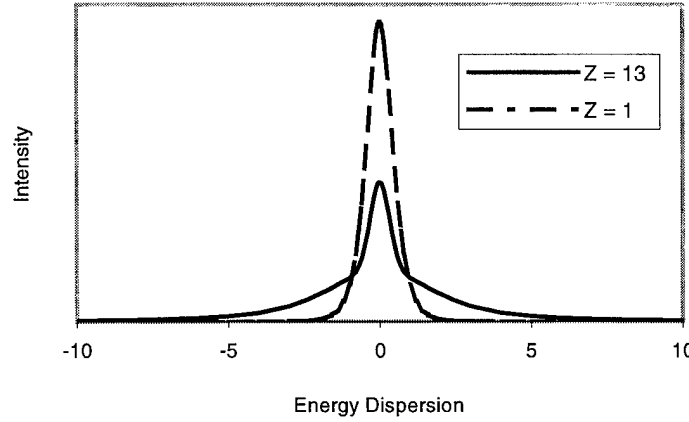

Figure 2-1. A comparison of the Compton (Doppler) broadening of hydrogen and aluminum. Both dispersion curves are for a single energy line (Plot provided courtesy of B.L. Evans)

The impulse approximation is often invoked to describe Compton broadened scattering [Namito, Matschenko, Ordonez]. This approximation relates the double-differential cross-section per differential solid angle dΩ per differential energy dE′ for a scattering angle θ (Equation 2-1).

$$\frac{d^2\sigma_s}{d\Omega dE'} = \frac{m_0 r_0^2}{2\sqrt{E_0^2 + E'^2 - 2E_0 E' \cos\theta}} \cdot \left(\frac{E'}{E_0}\right)\left(\frac{E_C}{E_0} + \frac{E_0}{E_C} - \sin^2\theta\right) \cdot J(p_z) \qquad (2\text{-}1)$$

where: m_0 – is the rest mass of an electron
E_c – is the recoil energy of the electron
$J(p_z)$ – is the Compton broadening profile of the scattering material
p_z – is the projection of the recoil electron momentum on the scattering vector

12

The Compton broadening profile is unique for each element, with dependence on orbital electron configuration. The dependence is in the number of electrons present in the orbitals. The effect of broadening is less severe at lower Z values, but a higher Z value causes a much greater dispersion. Therefore, hydrogen, having only a single electron in the 1s orbital, has the narrowest Compton profile due to the least amount of broadening. Aluminum has many more contributions of broadening from its 2s, 2p, 3s, and 3p orbitals. The more tightly bound electrons in aluminum have more momentum and thus cause more broadening.

Compton broadening has a severe impact on the MCST system's ability to measure energies down to the detector resolution (~500 eV). As Compton broadening is on the order of a few keV's, it is a greater source of energy dispersion than detector resolution. Thus, broadening becomes the greatest contributing factor in the reduction of the MCST energy resolution.

The Klein-Nishina differential cross-section. The Compton scattering equation does not take into account the photon-electron interactions. The Klein-Nishina relation provides the probabilities associated with the angles through which the photon will be scattered. The Klein-Nishina relation calculates the differential cross section (dσ) per solid angle (dΩ) for any angle (θ). Integrating the Klein-Nishina equation over all angles provides the total cross section. The form of Equation 2-2 is for scattering of unpolarized radiation from a free electron.

$$\left(\frac{d\sigma}{d\Omega}\right)_{KN} = \frac{1}{2}r_0^2\left(\frac{E'}{E_0}\right)^2\left(\frac{E'}{E_0} + \frac{E_0}{E'} - \sin^2\theta\right) \tag{2-2}$$

where: $d\sigma$ is the differential cross section
$d\Omega$ is the differential solid angle
r_0 is the electron radius
E' is the energy of the scattered gamma-ray
E_0 is the energy of the incident gamma-ray

While the Klein-Nishina formula assumes the electron to be at rest, the incoherent-scattering function, Equation 2-3, is a correction that incorporates the momentum of the electrons. This is one of the simplest forms for calculating the differential scattering cross sections.

$$\left(\frac{d\sigma}{d\Omega}\right) = \left(\frac{d\sigma}{d\Omega}\right)_{KN} S(x, Z) \tag{2-3}$$

where S(x,Z) is the incoherent scattering function that depends on Z (atomic number) of the element and on x which is defined as:

$$x = \frac{\sin\left(\frac{\theta}{2}\right)}{\lambda_0} \tag{2-4}$$

where λ_0 is the incident photon wavelength.

14

Scattergram Computational Model

The Scattergram computational model predicts the spectra of the singly scattered photons detected in the MCST. The model determines the probability of a source gamma ray to undergo a single scattering event in the sample and enter the detector array. The model provides a spectrum for each of the detectors in the array, given a specific geometry and sample description.

The code sets up a grid of pixels, in the image region containing the sample. Scattergram deterministically calculates the probability that a photon will scatter from a single pixel into a specific energy bin of a specific detector as shown in Figure 2-2. For each incident gamma-ray photon, the total probability of detecting a scattered photon of a specific energy in a detector is the summation of the scattering probability from all pixels. This probability includes both the scattering angle distribution as well as the energy distribution of the scattered photons. The imaging region is defined as the area that is both illuminated by the source gamma rays and located within the detector field of view. The modeled imaging region is smaller than the actual region to reduce computations.

Scattergram incorporates detector resolution, detector efficiency, Compton broadening, and attenuation of both the incident and scattered photons in the sample geometry, but does not take into account multiple or coherent scattering. Using fan-beam collimation to allow predominately single-scattered photons to enter the detectors validates this assumption. Finally, random Poisson noise can be applied to each of the modeled spectra.
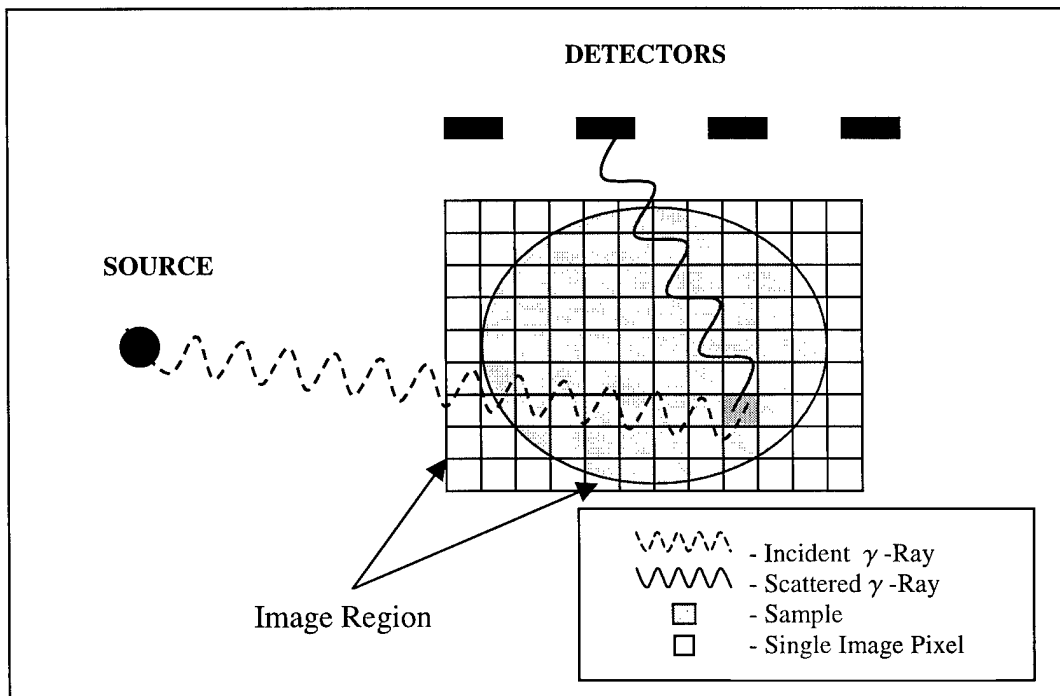
Figure 2-2. A visualization of the image grid developed by the Scattergram modeling program. The picture shows the attenuation and scattering of an incident photon off a single pixel in the sample.

The model assumes that the only calculates the probability of single Compton scatter. The other mechanisms (photoelectric absorption, coherent scatter) are included in the total attenuation cross section but neglects coherent scatter and any combination of multiple scatters. The contribution of this combination is assumed negligible. This assumption is valid when using photons at a low energy range in low-Z materials, i.e. when Compton scatter is the dominant interaction. Proper fan beam collimation of both the source and scattered radiation into the detector enhance this assumption. The values

used for the Compton scattering cross sections and total attenuation are entered into the code as polynomial interpolations [Evans, 1999].

The code is designed to account for only three materials, aluminum, air and bayerite. Bayerite is used to model corrosion of aluminum and is not needed for this project. Therefore, in this project, aluminum is used for all sections of the bone phantom (discussed in Chapter IV: Procedures).

Image Reconstruction

The purpose of the image reconstruction algorithm is to generate a two-dimensional image of the electron density. The reconstruction algorithm uses the energy data collected from the MCST to develop the image.

In the homogeneous bone phantom, the electron density is related to the mass density by a constant factor, thus the image is representative of the mass density. The reconstruction produces a 2-dimensional image of the phantom's electron density. Lower mass density appears as darker locations in the image, whereas greater mass density appears as lighter areas in the image.

In order to produce an image, the Compton profile is treated as a shift-variant point-spread function that blurs an "ideal spectrum". The "ideal spectrum" is the energy distribution calculated by the Compton equation (1-1) in each detector. This spectrum does not include the effects of Compton broadening, detector resolution, background or noise.

$$g - b = H f + n_g + n_b \tag{2-5}$$

where: **g** is the measured signal
      b is the measured background
      H is the matrix shift-variant blurring matrix
      f is the density of the sample
      n_g is the vector of statistical noise in the signal
      n_b is the vector of statistical noise in the background

The objective of the reconstruction algorithm is to recover an approximation to **f**

(**f** $\tilde{}$) from the measured signal **g** given **b** [Evans, *et al.* 1997]. The matrix **H** (i,j)

incorporates the detector resolution by convolving the normalized probabilities with a

Gaussian function by Equation 2-6.

$$H(E_i, \theta_j) = \frac{\left[\dfrac{d^2\sigma_s}{d\Omega dE'}(E' = E_i, \theta_j) \right]_{IA} dE'}{\displaystyle\int_0^\infty \left[\dfrac{d\sigma_s^{\,2}}{d\Omega dE'}(E', \theta_j) \right]_{IA} dE'} \qquad i \in \{1,2,...,N_E\}, j \in \{1,2,...,N_E\} \tag{2-6}$$

$H(E_i, \theta_j)$ is the probability that a photon will Compton scatter at angle θ_j with a detected

energy E_i. The presence of noise does not allow for the simple inversion of **H** to obtain **f**.

Evans has determined that the iterative technique of penalized weighted least

squares (PWLS) is superior to other techniques such as filtered back-projection [Evans,

1998]. PWLS allows for the reconstruction of the electron density distribution from the

data set $\Psi(j,k)$ which is the counts of Compton scattered photons collected in each energy

bin of each detector.

To use PWLS, a system map must be constructed, $A(\rho)$, whose element $A(i,m)$ relates the density in pixel m to $\Psi(i)$, the number of counts in a single energy bin of a single detector. The counts are calculated by subtracting the background counts from the measured data:

$$\Psi = g - b \qquad (2\text{-}7)$$

and the variance of the counts is:

$$\sigma_\Psi^2 = \sigma_g^2 + \sigma_b^2 \qquad (2\text{-}8)$$

which can be written as:

$$\sigma_{\Psi(i)}^2 = g(i) + b(i) \qquad (2\text{-}9)$$

The method minimizes the penalized weighted least-squares objective function:

$$\Phi(\rho) = \frac{1}{2}(\Psi - A\rho)^T \Sigma^{-1}(\Psi - A\rho) + \beta R(\rho) \qquad (2\text{-}10)$$

where: Σ is the diagonal matrix with $\Sigma_{ii} = \sigma_{\Psi(i)}^2$.

The first term of the objective function is the least squares similarity measure, and encourages agreement between the image and the measured data. The $R(\rho)$ term is a regularizing penalty function that encourages agreement between neighboring pixels and, therefore, prevents oscillatory solutions. The parameter β controls the tradeoff between these two terms. In order to correct for particularly noisy measurements, an increase of β will cause a more stable solution but will also reduce image sharpness [Evans, 1999].

The image iterations of MCST depend on the convergence of ρ and the system matrix $A(\rho)$. This demands two levels of iteration, an "inner" iteration for ρ and an

"outer" iteration for the system mapping $\mathbf{A}$. For the solution to be achieved, for each new $\mathbf{A}$, the ρ iteration is repeated until the density converges.

The method of successive overrelaxation (SOR) is used during the inner iteration to minimize the objective function. The relaxation constant ω controls the convergence rate of the solution. Using a value of $\omega < 1$ incorporates the lower frequency components, while using an $\omega = 1$ incorporates the higher frequency components [Evans, 1999].

III. EQUIPMENT

The primary pieces of the Multiplexed Compton Scatter Tomograph (MCST) used in this project are the detector array, source, collimators, signal processing system, and the display software. This chapter describes each section of the MCST.

Multiplexed Compton Scatter Tomograph

The primary machine used was the MCST located at AFIT. The detector array was built by Princeton Gamma-Tech, Princeton, N.J. and consists of a single array of six high-purity germanium (HPGe) crystals aligned in a planar geometry (Figure 3-1). The active volume of each detector is 800 mm^3, containing an active front area of 80 mm^2. The front area, or aperture, of each detector is open to the sample. The apertures are covered with a 0.25 mm thick beryllium foil that has an area of 78 mm^2. The detectors have a 1.96 cm space between them (Figure 3-3).
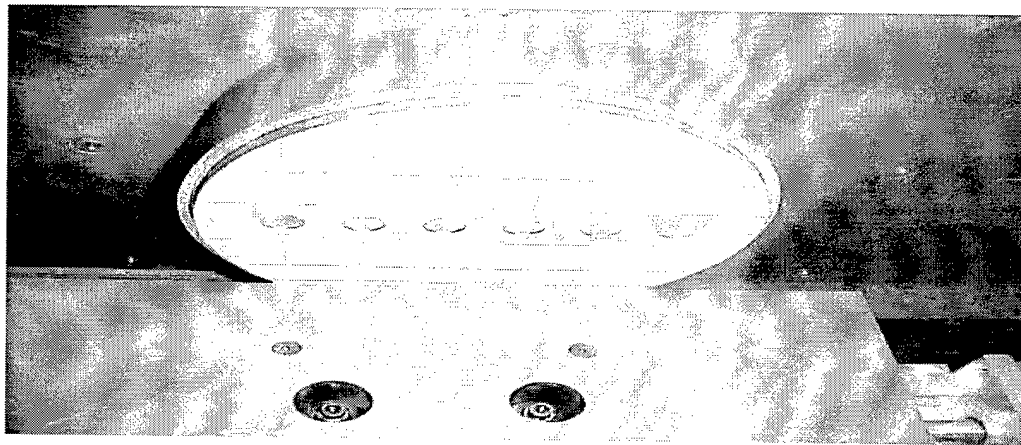

Figure 3-1. A picture of the HPGe detector windows in front of the position plate (foreground). Both the windows and the positioning plate are enclosed in a tin box for γ-ray absorption.

An aluminum end cap is between the HPGe crystal and the beryllium window. The crystals are set back 3.5 mm from the window, thus confining each detector's effective field of view. As a single detector has a viewing cone of approximately 40 degrees from normal, shown in Figure 3-2. For this project, the physical impact is that no more than four detectors are able to view a sample. Data collection, sample size and placement are subsequently affected. Specific impacts are discussed in Chapter IV: Procedures.
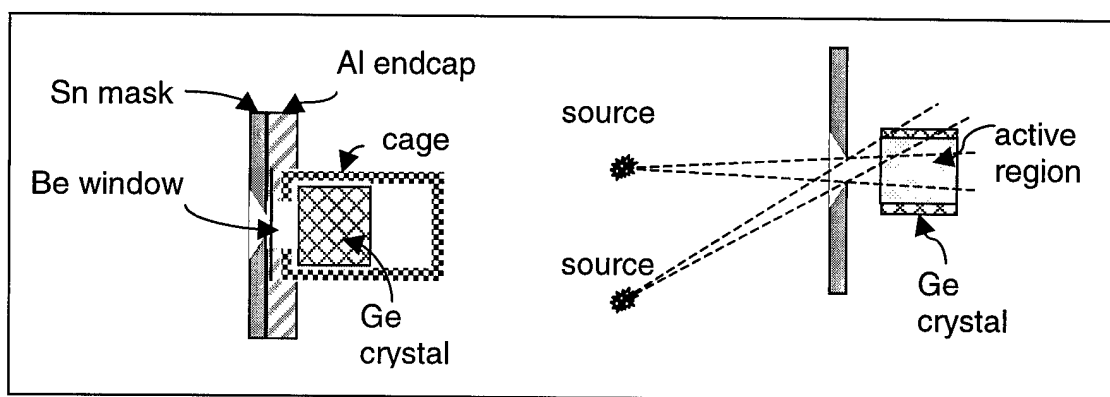

Figure 3-2. A single MCST crystal design. The figure shows the limited field of view of each detector crystal. (Provided courtesy of B.L. Evans)

The detectors have a voltage bias of +1500 volts. The cryostat that houses the detectors is passively cooled by a liquid nitrogen-filled dewar in order to reduce noise and increase energy resolution.
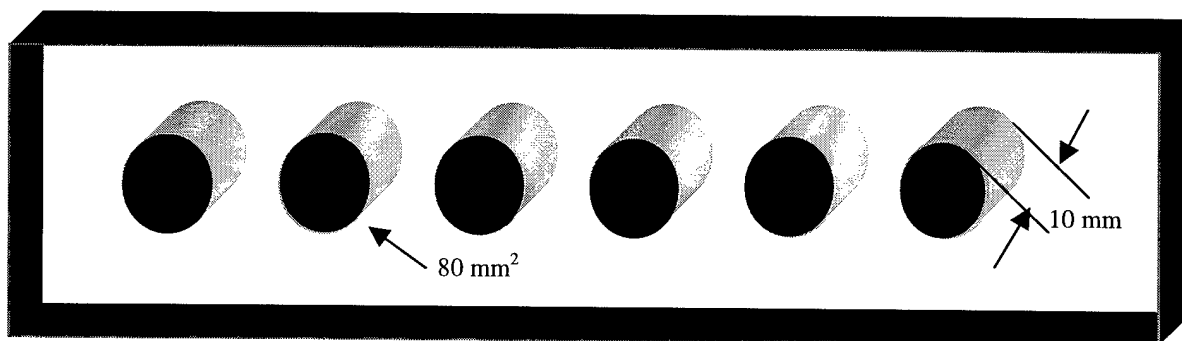

Figure 3-3 The planar array of identical HPGe detectors, with dimensions of the active volume. The black fronts represent the areas open to incident photons.

Detector energy resolution defines the range of energies over which a single

energy line is spread or blurred. The average energy resolution for the six detectors is

375-532 electron volts (eVs). Table 3-1 contains the specific energy resolution

information for each detector at the energy range of interest (60 keV-90 keV). The

modeling and image reconstruction codes consider the energy resolution of each detector,

as discussed in Chapter II: Theory.

Table 3-1.
The Energy Resolutions for the MCST detectors

Detector Element	Energy Resolution In electron volts at 59.54 keV / 88.03 keV
1	375 / 384
2	405 / 494
3	390 / 452
4	408 / 420
5	489 / 451
6	495 / 532

Calculating the full-energy efficiency was also critical for characterizing each

detector. Energy efficiency quantifies the capability of each crystal to detect each full-

energy photon incident on the crystal. The full-energy efficiency plots of the detector

array in Figure 3-4 depict this behavior. Although it is desirable to have as close to 100%

efficiency as possible over the energy range, it is more important to have the systems

response to the efficiency properly modeled.

The angular dependence of each detector is quite severe. The angles of incident

limit the amount of photons that enter the detector. Figure 3-5 shows the reduction of

intensity as the incident angle increases from normal. This figure shows that the

limitation of the detector field of view is approximately 35-40 degrees from normal.
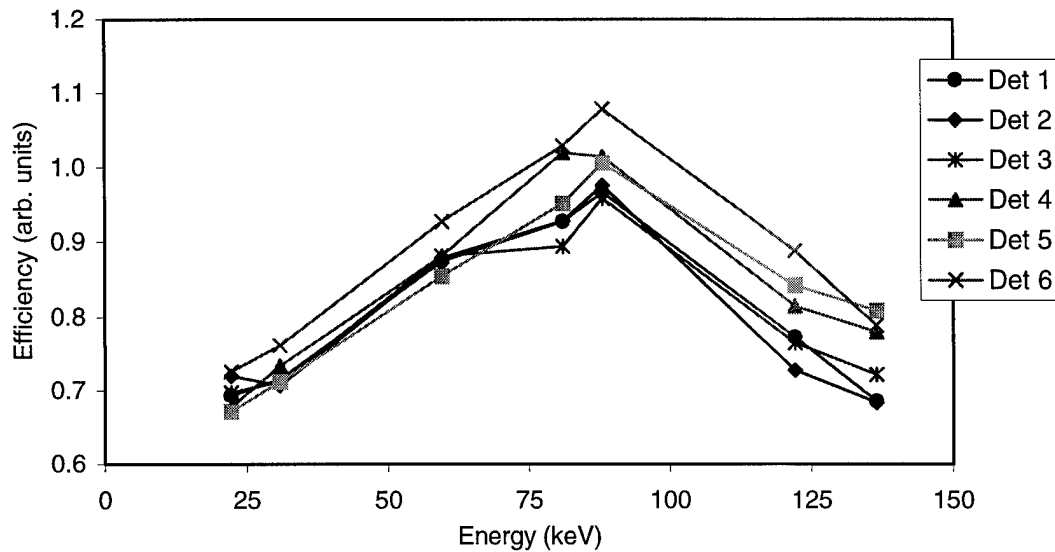

Figure 3-4. Full-energy efficiency curves for all MCST detectors.
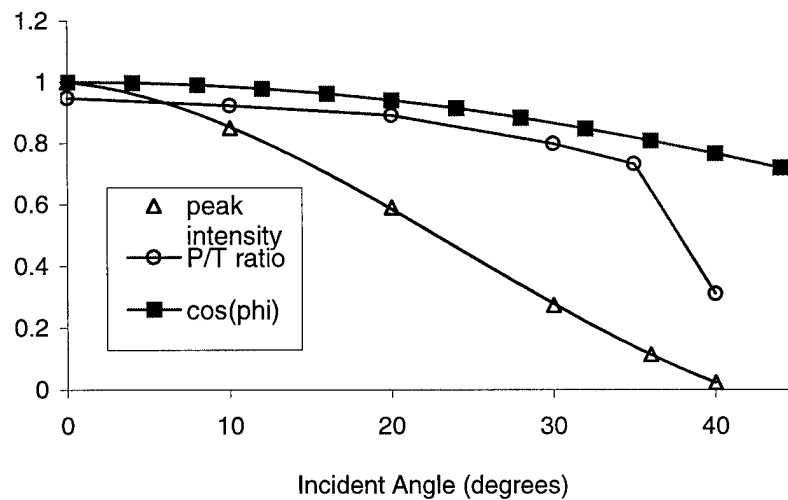(Provided courtesy of B.L. Evans)

Figure 3-5. Peak to total energy ratio. This ratio shows the reduction as a function
of angles from normal on the detector. The triangle is the peak value recorded,
the circle is the peak-to-total ratio for the detector, and the square is the cosine of
the angle. (Provided courtesy of B.L. Evans)

Source Collimator

For this project, a special source collimator was fabricated, whereas a previously designed collimator was used in front of the detectors. The source collimator shapes the source gamma rays into a uniform fan beam to reduce the illumination volume on the phantom. The detector collimator reduces the effective slice thickness imaged by the MCST, thereby reducing contamination by multiple scattering events. The collimator also serves to restrict the imaging region to a plane, which makes image reconstruction by the previously described method possible. The source collimator is perpendicular to the detector collimator so that the scattering angle from the phantom is approximately 90 degrees. Figure 3-6 shows both collimators and phantom. The symmetry of this geometry provides advantages for data manipulation as discussed later in Chapter IV: Procedure. This also parallels clinical systems that measure completely around a patient's appendage (an arm or leg, for example).
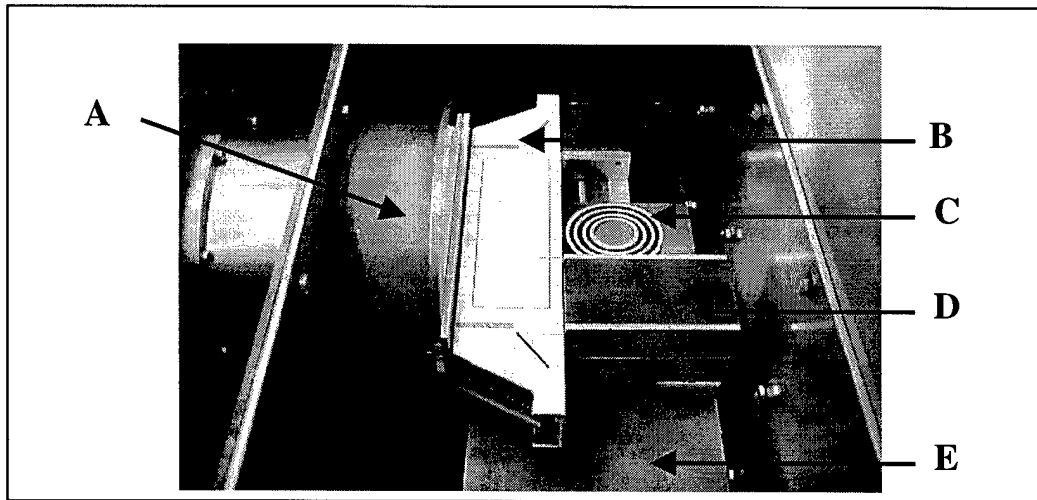

Figure 3-6. Photograph shows the geometry of the system with both collimators and a phantom in place. The diagram on top of the detector collimator allows for consistent alignment of the source collimator and the phantom. The items listed are A - detector cryostat, B -detector collimator, C –phantom, D – source collimator, and E positioning plate.

Although an original source collimator exists for the MCST, an additional collimator had to be built specifically for this project. One major limiting factor of the original purpose of the MCST was to limit the source and detector array to the same side of the sample. However, in this project, this is an unnecessary limitation; so a new geometry was developed that required the fabrication of a new source collimator.

The source collimator consists of tin plates that allow only a thin fan beam of source radiation to pass. Tin is an effective absorber of 88 keV gamma rays, preventing scattering off the collimator. The tin plates are fastened to a steel frame, which is, in turn, fastened to a Plexiglas stand as shown in Figure 3-7. Appendix D shows the schematic drawings used to fabricate the collimator. Pure tin is extremely soft and malleable, so support from the steel structure ensures reliability and durability during the experiment. In addition to the front and rear plates, tin also lines the internal steel structure to prevent scattering from inside the collimator.

The width and alignment of the slits are very important to the collimation of the source radiation. The front and rear widths are 2 mm, and are aligned to within 0.2 mm. The maximum divergence of the source fan beam is approximately 13 mm at the far end of the phantom, 9 cm from the source. By using the existing detector collimator and the new source collimator, a thin slice can be imaged with a reduction of multiple scattering.

One of the consequences of reducing the width of the source collimator is reduction of the number of photons reaching the phantom and thus scattering into the MCST. Although narrowing the source and detector collimation helps ensure that singly scattered photons are dominant, a tradeoff exists between multiple scatter contamination and reasonable data collection times.
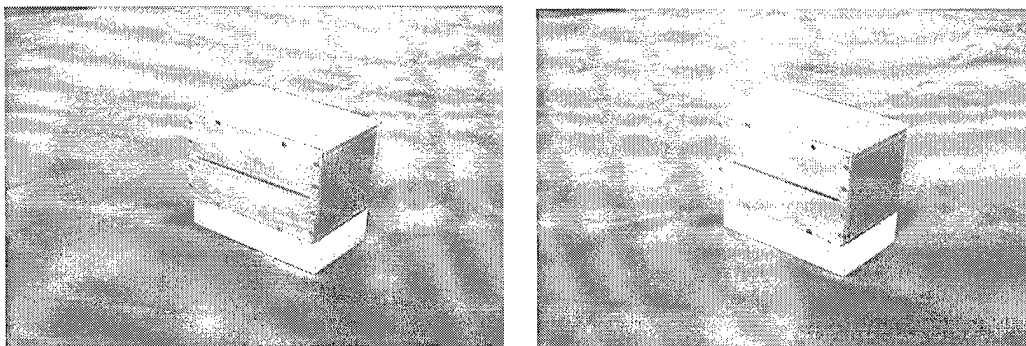
Figure 3-7. Image of the source collimator. The collimator is tin bolted onto a steel structure for strength with a Plexiglas stand for proper alignment.

Signal Processing System

The signal processing units convert the signal from the detectors into digitized

pulse heights, display the data, and record the data for further analysis. The circuit

diagram is shown in Figure 3-8. The signal originates in the MCST when a photon enters

the collection window of HPGe crystal, deposits its full energy within the crystal, and is

collected by the internal electronics. This signal travels to the Dual Spectroscopy

Amplifier, which provides pole-zero cancellation while shaping and amplifying the pulse.

The signal splits to a Delay Amplifier and a Timing Single Channel Analyzer (T-SCA).

The Delay Amplifier again increases the magnitude of the signal and adds a slight delay

so the arrival of the pulse information is coincident with the timing information from the

T-SCA. The timing signal provides a gate signal to the Analog-Digital Converter (ADC)

which tells it to perform the conversion. The 8-Channel Peak Detection Module receives

the analog pulse, accomplishes the conversion and then sends the digital signal to the

computer display. The digitized signal passes to the display and recording software, the

Multi-Parameter CAMAC Data Acquisition System (*Multi*). Note that the software is

capable of recording the clock time of the event but no timing information is recorded or
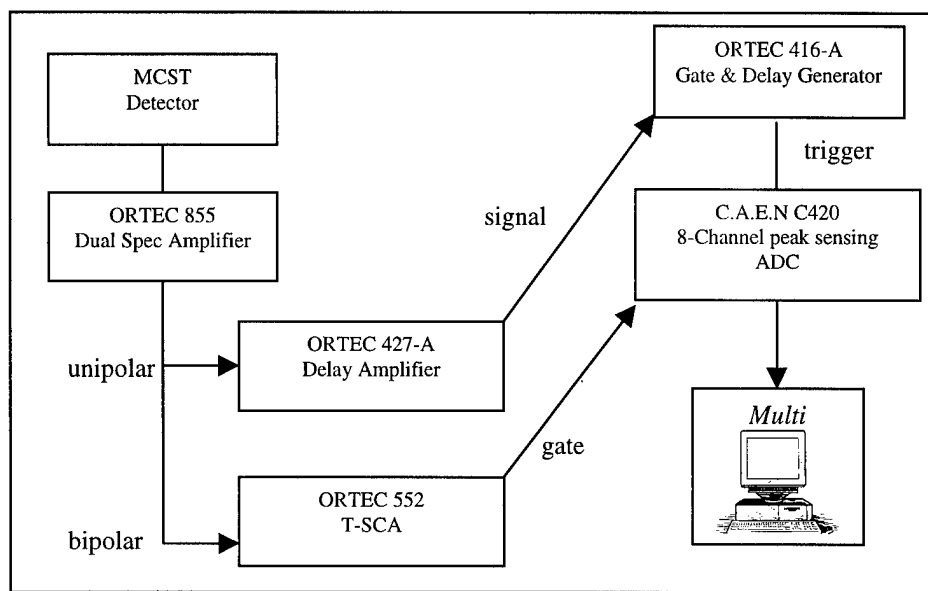
utilized for this project.

Figure 3-8. Circuit diagram of the signal processing system.

The units are standard CAMAC (Computer Automated Measurement and Control) or NIM (Nuclear Instrument Module) components. A CAMAC crate houses and supplies power to the modules as shown in Figure 3-9. A Weiner CC16 Crate Controller [Plein 1994] provides an interface for the user to control and configure all the modules through a desktop computer. The controller receives start/stop and detector configuration information from the user via the *Multi* software. *Multi* was used to provide experiment control, file management, operation monitoring, archiving and graphic display of the data. Although *Multi* contains some analysis tools, all processing and analysis occurred off-line with the help of *Microsoft Excel* spreadsheets.
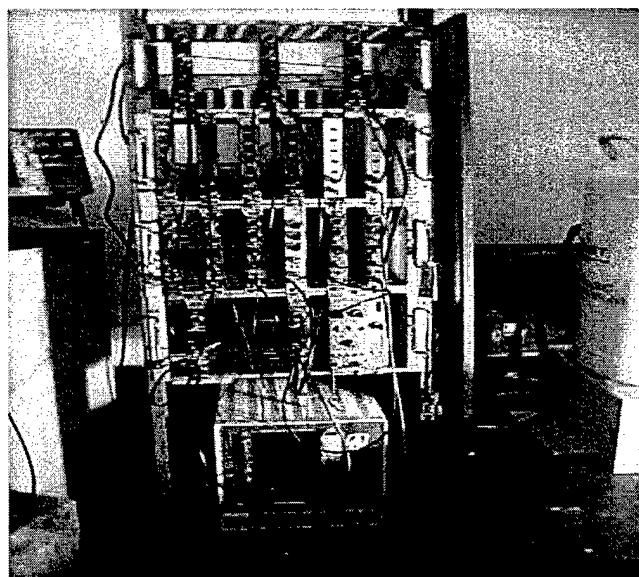
Figure 3-9. The entire CAMAC system used for signal collection and processing.
(Provided courtesy of B.L. Evans)

IV. PROCEDURE

This chapter describes the procedures of the project. The procedures started with the design and fabrication of the bone density phantom and the source collimator. The next step was to model each phantom with the Scattergram computational code. Data was then collected on each phantom. The modeled and detector energy spectra were used to generate images of the phantoms. The final step was to compare the detector images with the modeled images.

Bone Density Phantom

I used synthetic materials to build a model that represents the typical size, geometry and density of bone and surrounding soft tissue. I investigated clinical phantoms from Miami Valley Hospital and Wright-Patterson Medical Center as well as phantoms published in the literature [Hangartner, 1999] as a template for my design. Although the basis for my design came from these accepted phantoms, my final design was unconventional due to developmental and manufacturing limitations.

Clinical phantoms accurately represent the proper mass density of bone in a human subject, Figure 4-1. Aluminum is used to model the hard cortical bone, and Plexiglas has been found to have the appropriate density to represent bone marrow. The soft tissue can be modeled with water. Table 4-1 shows a viable solution to developing a bone density phantom. A typical phantom might have an interior trabecular volume filled with Lucite, encased in a thin layer of aluminum, and surrounded by an additional shell of water or water equivalent material.
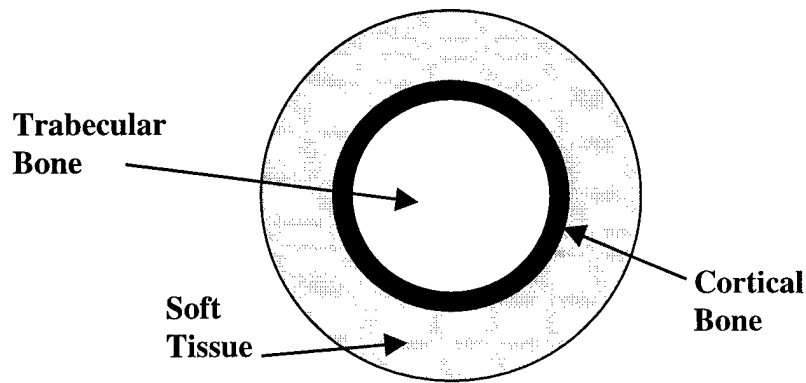
Figure 4-1. A cross-sectional view of a clinical phantom. The proportional dimensions are for an arm bone, although only a single bone is simulated.

Table 4-1. Materials commonly used to represent the human body

Anatomical Region	Actual Density [g / cm³]	Homogeneous Material used	Material Density [g / cm³]	Electron Density [Electron moles / cm³]
Marrow Bone	1.22	Lucite (Plexiglas)	1.22	0.658
Cortical Bone	2.7	Pure Aluminum	2.7	1.290
Soft Tissue	~1.0	water	1.0	0.555

The choice of materials was dictated by a restriction in the Scattergram modeling code. The code is able to model multiple densities of only a single homogenous material. This restriction forces the entire phantom to consist of aluminum and air. The aluminum is used to make all three regions of the phantom - the inner trabecular bone, the shell of the cortical bone, and the soft tissue surrounding the bone. This is accomplished by creating reduced density aluminum in the required regions.

The cortical bone density consists of normal density aluminum, while the soft tissue region is half-density. The trabecular region will be either half-density or approximately quarter-density aluminum. These two values represent the normal and osteoporotic densities of trabecular bone, respectively.

The soft tissue region of the phantom is an incorrect density. The phantom has a soft tissue region that has alternating rings of aluminum. There is no differentiation

31

between the soft tissue rings of 2 mm aluminum and the cortical shell of 2 mm. This problem causes significant errors with the phantom. The density of the soft tissue is approximately 1.0 g/cm^3. In the phantom, the density is 1.3 g/cm^3. This error causes the soft tissue to be over represented with material, and creates a higher attenuation of the incident fan beam. This error was not realized in time to recreate an additional phantom. Instead of an electron density of 0.555 electron moles per cm^3, this project's phantom depicts a 35 % density increase with a density of 0.658 electron moles per cm^3.

Clinical credibility was a critical driving force in the phantom development. Proper clinical representation of both the relative and absolute dimensions was essential, regardless of the materials used. Without the proper dimensions, any results would be inconclusive in regards to the ability of the system to determine variations in the trabecular bone density. The issue of the soft tissue density being too high, and the cortical shells not significantly different from the soft tissue shells cause the focus of the results to be on the trabecular region only.

In addition to modeling and physical accuracy considerations, there were also material acquisition and machine limitations. Obtaining large amounts of pure aluminum in a manageable form proved difficult. Pure aluminum is a very soft and malleable metal that is difficult to machine into thin sheets. The design could not demand extremely thin regions of aluminum during fabrication. Each region had to be no thinner than 1 mm to prevent rips or tears when built.

The phantom stands 25 mm tall supported by a 20 mm high Plexiglas block, as shown in Figure 4-2. Appendix C shows the schematic drawings used to fabricate the phantom. The phantom has a 49 mm outer diameter and a 19 mm interior diameter. In

the outer-most region, concentric aluminum shells represent the soft tissue. Each shell is 2 mm thick, with a 2-mm radial gap between them. Due to the MSCT resolution of approximately 3.2 mm, these gaps will not be detectable. The next section, the cortical region, is adjustable with a thickness of either 2 mm or 3 mm. Both of the cortical shells have an inner diameter of 19 mm to accommodate the trabecular cores. The various cortical shells represent different body types and their corresponding bone thickness.
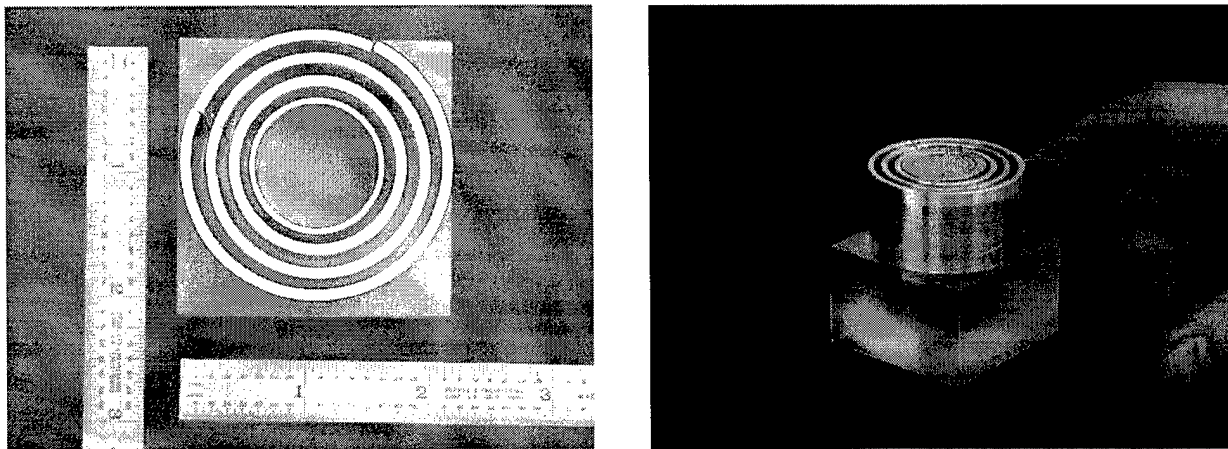
Figure 4-2. Photographs of the phantom. The phantom consists of aluminum shells placed on a Plexiglas stand for proper alignment.

To detect changes in the trabecular bone density, the inner core of material can be varied to achieve three different electron densities. The three densities are of normal bone density, osteoporotic bone density, and a void in the trabecular region. Table 4-2 shows the densities used for each of the regions. A 1350 alloy, 30-mesh aluminum was used to lower the aluminum density to the appropriate electron density in the trabecular region. The 30-mesh designator means that the material has 30 holes per inch using a 0.012 inch diameter wire. 1350 alloy represents 99% pure aluminum with 1% undefined contaminants.

Table 4-2. MCST bone phantom densities for various types of tissue.

Phantom Location	Mass Density (g/cm^3)	Electron Density (Electron moles / cm^3)	% difference from clinical values
Trabecular – Normal	1.38	0.659	0.15 %
Trabecular – Osteoporotic	0.826	0.395	-----
Soft Tissue	1.35	0.645	35 %

To represent the normal region of the trabecular density, the density of the mesh alone was too low for proper characterization. Additional full density, 1100 alloy (99.99% pure) aluminum disks were added to the stacked mesh core. The disks increase the electron density in a region. The source fan beam is approximately 13 mm thick, within which thickness small density variations can not be resolved. Each disk is 2.0 mm thick and placed such that any 13 mm slice will represent an electron density of 0.659 electron moles / cm^3 as shown in Table 4-2. This adjustment to the aluminum mesh is adequate for the MCST image due to the thick imaging slice, but is inappropriate when measuring the phantom with the computed tomography (CT). Measurements with the dual-energy x-ray absorptiometry (DEXA) system can be averaged to provide appropriate integrated values.

The osteoporotic core contains vertically stacked pieces of aluminum mesh. The density of this configuration appropriately reflects a 40 % decrease from normal trabecular density. This is adequate to determine if the MCST is capable of discerning the difference between osteoporotic and normal trabecular electron density.

In Table 4-2, the clinical values for the normal trabecular bone and the soft tissue were derived from literature. Lucite, $C_5H_8O_3$, is frequently used to represent bone

marrow [Hangartner, 1999]. Using this fact, I calculated the electron density of Lucite, and defined that value as the clinical values for those regions. There is no comparison of the osteoporotic density in the table since there is no single value when a bone changes from being normal to osteoporotic. Osteoporosis is clinically defined as a decrease in bone density. This decrease is dependent on other factors such as age, sex, and race. However, values of 40% and more below the density of normal subjects are considered osteoporotic. Therefore, no single value is used in Table 4-2.

The problem resulting from the improper representation of soft tissue is discussed further in Chapter V: Results and Discussion.

MCST Point Spread Function

A calibration of the Scattergram code involved measuring the point spread function (PSF) within the imaging region. A 0.635 cm aluminum bar simulated a point source (of scattered photons) in nine positions throughout the region, as in Figure 4-3. These adequately simulate point sources due to the low spatial resolution of the system. Each PSF modeled position required scaling to the actual data, with each position using a different scaling factor. The Scattergram spectral output is a set of probabilities of scatter from each pixel into a specific energy bin of a detector. In order to relate this to the scattered photon counts detected, the probabilities are multiplied by a scaling factor. Therefore, this is less an arbitrary correction than a scaling mechanism since the model spectra is a set of probabilities and not counts directly.

The nine-point grid of scaling factors was modeled by a polynomial interpolation. This relation produces a shift-variant correction to account for locations that are not

weighted properly relative to surrounding pixels. The reason for the weighting factor is due to an unknown error in the Scattergram simulation code. The Scattergram model incorporates the polynomial correction to adjust the imaging region as shown in Equation 4-1. In the incorporation of the polynomial correction, the reference values had to change due to the rotation of the source-detector array positions. This is equivalent to scene registration used in visual imaging. Appendix A contains the specifics on data collection and analysis of the PSF data.

$$
\begin{aligned}
&1.41 + 7.46 \times 10^{-3} x - 2.18 \times 10^{-2} x^2 + 2.57 \times 10^{-2} x^{-3} + \\
&8.84 \times 10^{-4} y - 4.61 \times 10^{-2} xy + 7.11 \times 10^{-3} x^2 y + 2.71 \times 10^{-2} y^2 - \\
&1.02 \times 10^{-2} xy^2 - 2.81 \times 10^{-3} x^2 y^2 + 1.92 \times 10^{-3} y^3
\end{aligned}
\qquad (4\text{-}1)
$$
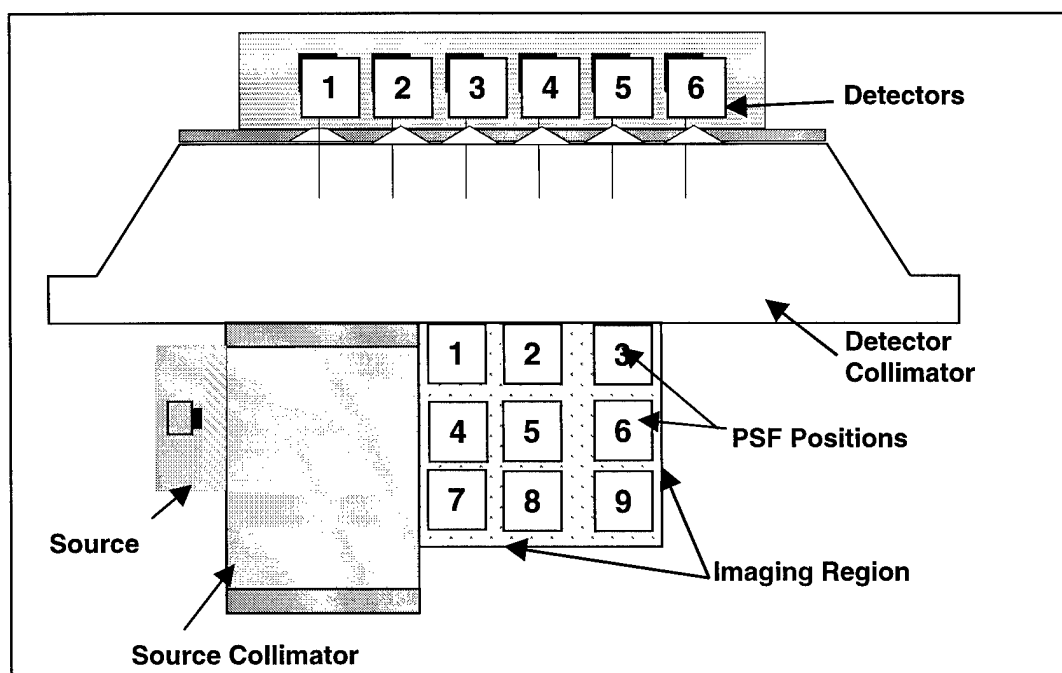
Figure 4-3. The collection layout of the nine positions used to measure the point spread function of the system. The nine locations mark the imaging area where the phantom will be positioned.

Phantom Measurements

In this project, four phantom designs were imaged in the MCST. The combinations used in the phantoms give a wide range of bone densities. All phantoms in Table 4-3 contain the same soft tissue region.

Table 4-3. A description of the phantoms imaged by the MCST.

Phantom	Cortical Bone Thickness	Trabecular Bone Mass Density (Grams / cm^3)	Trabecular Bone Electron Density (Electron mole / cm3)
Thin - Void	2 mm	0.0	0.0
Thin - Osteoporotic	2 mm	0.826	0.395
Thin - Normal	2 mm	1.38	0.659
Thick – Osteoporotic	3 mm	0.826	0.395

Data for each phantom was collected at three different positions relative to the detectors. For each position, the phantom was moved forward one-third of the distance between the detectors, i.e. 0.635 cm. Due to the detector size, multiple positions allow better discrimination of the location of scatter. Figure 4-4 shows the location of the phantom edge for the three positions relative to the detector array.

37
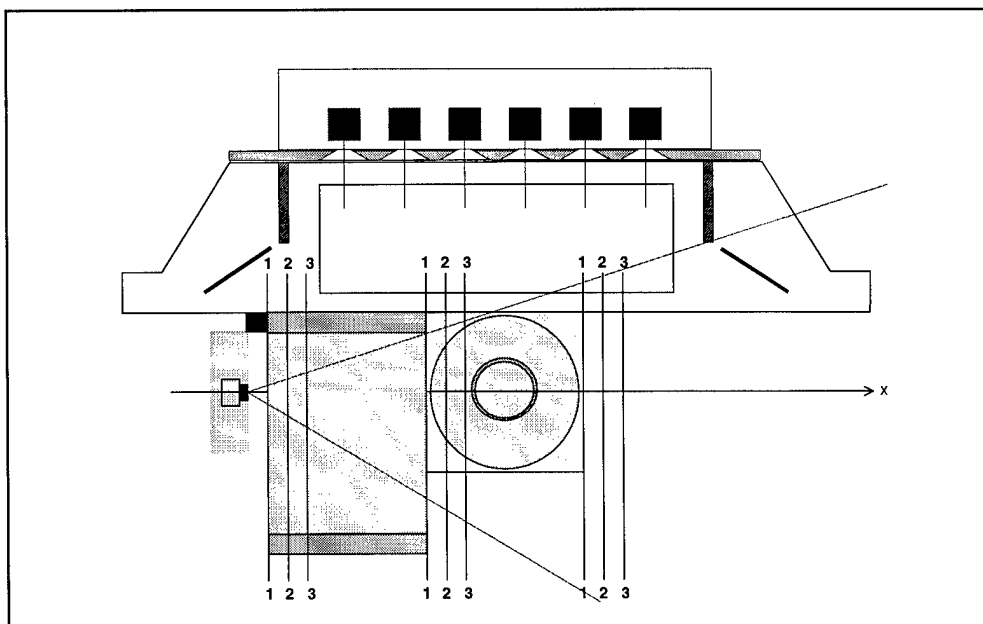
Figure 4-4. Picture of the positions used for the data collection. The configuration shown is for position-1. The subsequent data sets are measured after moving the source, source collimator, and phantom along the x-axis to the designated line.

The MCST collected 12 hours of data for each phantom at each position. This time was based on previous images created by the MCST and on the time the MCST was available. One data collection, the 2 mm shell with a void center, extended over 16 hours for each position. This should allow for some comparison between the images based on different collection times.

Simulations

The Scattergram code was used to predict each spectrum collected by the MCST. Each phantom was modeled at each of the collection positions. The simulation code provided a comparison tool to examine the data collected from the MCST. This comparison consisted of shape and relative amplitude evaluation [Evans, 1999].

Besides spectrum analysis, the Scattergram code provides an essential component to image generation. The code develops a matrix that maps the electron densities (ρ) to the energy spectral measurements (Ψ). The reconstruction program must have this initial estimation of the map in order to produce the final image.

In the simulation, the phantom was surrounded with detector arrays as shown in Figure 4-6. The simulation used four source positions, with a total of eight detector arrays (two per source position). The two sets of data were to simulate position-1 and position-2 of the actual data sets. Currently, the image reconstruction algorithm is unable to incorporate more than eight detector arrays.
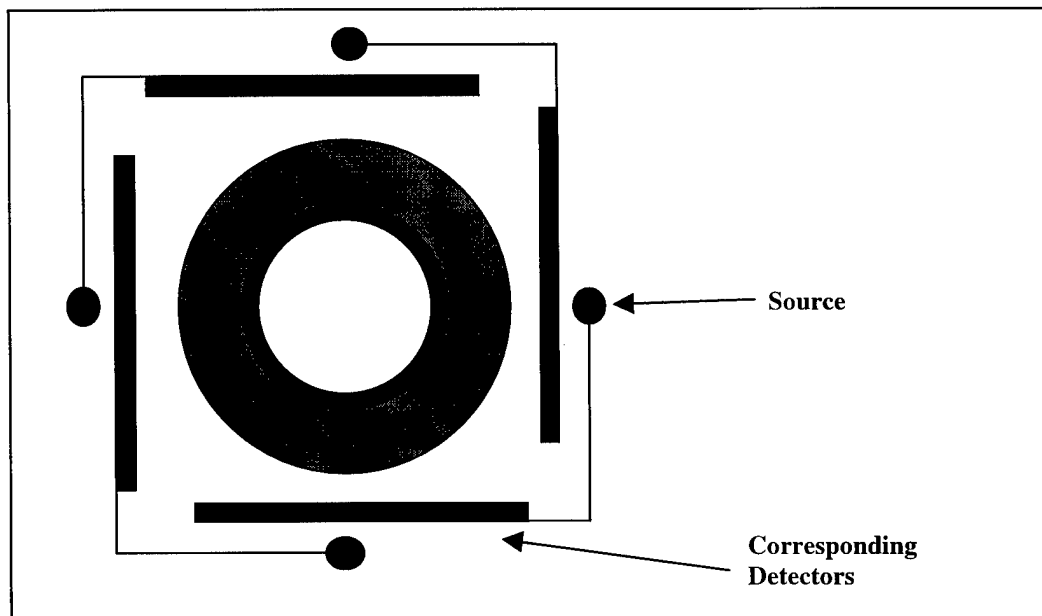
Figure 4-6. This graph shows the addition of artificial detectors. Duplicating the original data set, and assigning new positions to the detectors generates data from the additional detectors. This is used to improve image quality of the phantom.

Data Processing

The output of the MCST is a list of photons detected per energy channel for each

detector. The channels can be converted into energy bins by applying calibration data.

In order to reduce the size of the data, I used a *MATLAB* program to redistribute the data

counts into larger energy bins, from 0.06 to 0.2 keV per bin. An advantage of rebinning

to larger energy bins is to decrease the statistical uncertainty. This also allows a more

manageable data file size with no impact on image quality, since the larger bin size is still

below the detector energy resolution.

I used *Microsoft Excel* spreadsheets to apply the calibration information, to

perform background subtraction, and to display the data. This allowed a visual

interpretation when comparing the Scattergram predictions to actual data. Figure 4-7

shows the graphic comparison between the model and MCST data for a single detector.
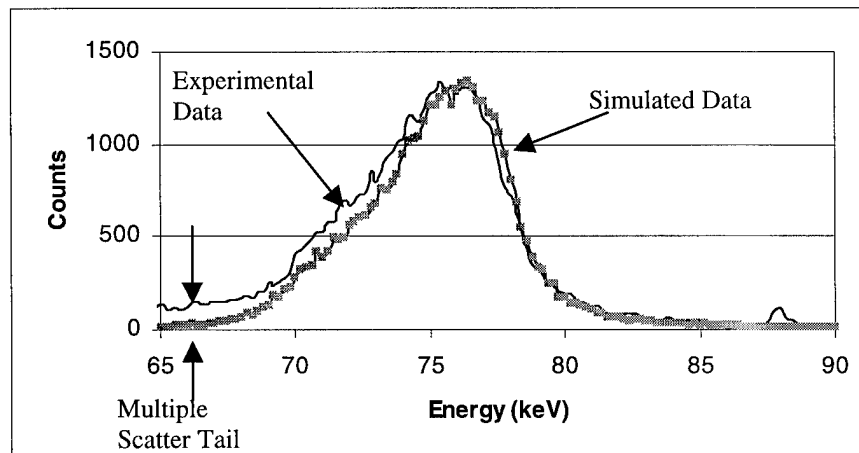
Figure 4-7. This plot is a comparison of actual detector data versus simulated data. Shown is detector 3 of the thin cortical shell configuration with a void center. The solid line is experimental data and the symbols represent the simulated data. The tail in the experimental data shows the contribution of multiple scatters. These are neglected in the simulation.

Image Reconstruction

Problems arise with reconstructing a complex sample without adequate angular information in the spectral data. The angular information required comes from the various source and detector positions surrounding the phantom. This increased number of positions provides higher fidelity in the resulting image. Due to symmetry in the data, I was able to simulate having a second set of detectors directly across from the original detectors such that the detectors surround the bone phantom (Figure 4-6). This doubled the data set. The duplicate set is a rotated image of the original and no additional manipulation is needed.

In doing this duplication, the noise attributed to the data set is also copied. The consequence is that the noise is no longer random, but has statistical correlation. However, since there were time restrictions to gather the vast amounts of data required, duplication of the data was preferred with the knowledge that possible consequences could result. The consequences of the duplication are not investigated in this project.

Finally, the image reconstruction algorithm used the total data set for each phantom to recreate the images. The reconstruction code enabled a quantitative (but not absolute) analysis of each of the phantom designs.

V. RESULTS AND DISCUSSION

This chapter is devoted to evaluating of the Scattergram computational model to predict the spectra and showing results of the MCST laboratory measurements. The laboratory measurements were used to create images of the phantom. The images are compared to images using simulated measurements. Measurements were also taken on a clinical CT scanner from Miami Valley Hospital.

CT Scanner Results

The CT scanner was used to measure all three densities of the phantom. The values of the normal and osteoporotic densities obtained from the CT scanner are shown in Table 5-1. Due to a slice thickness of only 1.2 mm, the CT scanner measured the aluminum sheets or the aluminum mesh placed in the center of the phantom [Hangartner and Overton, 1982]. This narrow beam is too fine for the phantom developed for the MCST. The phantom was developed to have an average density based on an incident beam dispersion of 1.27 cm.

Table 5-1. Bone Density Results from CT Scanner. Each measurement was repeated by moving the phantom 0.5 mm.

Data Set (Trabecular Density)	Average Relative Percent of Aluminum (Measurement #1 / #2)	Average Density (gram / cm³)
#1 (Normal)	.2412 / .2513	0.665
#2 (Osteoporotic)	.2456 / .2627	0.687

In Table 5-1, the thin fan beam resulted in the CT scanner measuring the aluminum mesh in both phantoms. This observation was made both with the visual

location of the cross-section, as well as inspecting the data. Had the fan beam been located in the full aluminum disks in the normal density, the density would have resulted in a much higher density (approximately 2.7 g/cm^3). Therefore, both data sets were measuring the aluminum mesh. Each data set consisted of two measurements.

Calculations related the density of the trabecular volume to that of solid aluminum. This allowed for a direct calculation of the measured electron density.

The differences in the measurements are likely due to non-uniform compression of the aluminum mesh in the phantom. The incident gamma rays may be passing through a slightly bent mesh, which creates an artificial gap. Again, such variations are not evident in the MCST, but the CT scanner is able to resolve the inhomogeneities in the phantom.

Scattergram Computational Model versus MCST Data

The Scattergram simulation accurately predicted the relative amplitudes of each spectrum for each phantom after correction with the polynomial. However, there is a slight deviation in the shape of the spectra. The difference in the shape can be attributed to poor calibration and contamination from multiple scattering. Calibrations were taken before and after each 12-hour data set. However, periodic measurements showed occasional drifts up to 10 channels (0.6 keV) in a matter of hours. Each data set was slightly adjusted to fit the 88 keV coherent scatter peak to the correct energy. The contribution of multiple scattering is manifested as counts in the lower energies, as is shown in Figure 5-1; the detector data do not go to zero at approximately 65 keV as the simulation predicts.

In Figure 5-1, measurements from a single position are shown for the thin cortical

shell with a void center (Thin-Void) phantom. The model is in good agreement in both

shape and amplitude. This spectrum is one of the best agreements of the two data sets.

Appendix B contains the compilation of spectra for all phantoms.
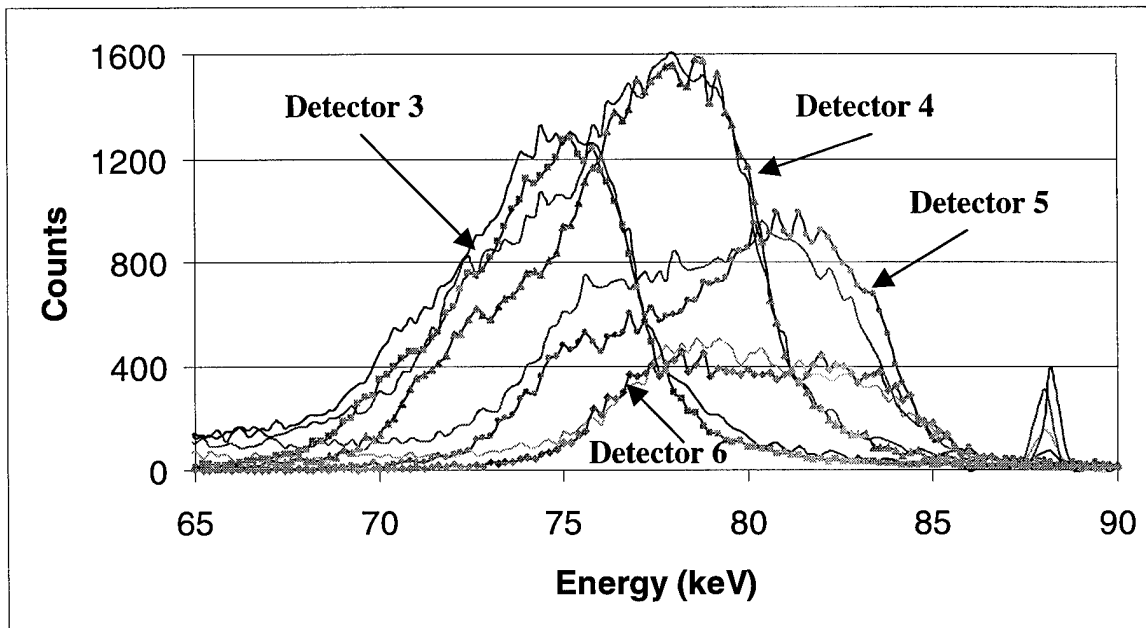
Figure 5-1. Spectral data. The spectra of the MCST data for the phantom with thin
cortex and center void along with the corresponding ScatterGram simulation of the same
phantom. This is one of the best agreements between the two data sets. The simulated
data is represented by symbols.

Image Reconstruction

The phantom spectral data collected by the MCST were reconstructed into a

2-dimensional image. The resulting images show a scale of values of density that is

proportional to the electron density. The image reconstruction requires an initial guess of

the phantom design. For this application, it is fair to assume some prior knowledge of the

patients bone size. The surrounding tissue, cortical and trabecular region densities can be

assumed by using values corresponding to healthy bone. This approximation allows the iterative image reconstruction to develop the final image by using the energy data. The initial guess used for all cases of the reconstruction is shown in Figure 5-2.
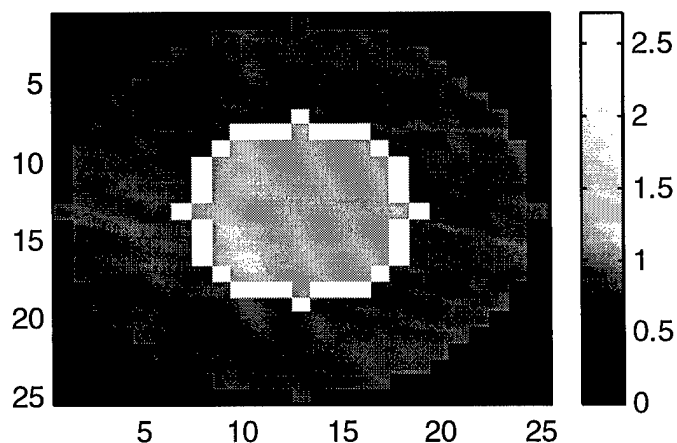
Figure 5-2. The initial density guess of bone phantom. This initial guess shows the density of a normal trabecular bone.

For each phantom, four detectors collected spectra at three different phantom positions. However, due to the large amount of aluminum used in the phantom, attenuation of the source is extensive. The mean free path of 88 keV photons in aluminum is 2 cm (attenuation coefficient of 0.1892 cm^2/g). Therefore, the compiled image is good for a quadrant of the phantom but, due to attenuation, the entire phantom can not be resolved. Table 5-2 shows the amount of attenuation that occurs in the phantom at various locations. The table assumes an incident energy of 88 keV, and assumes a scattered photon energy of 75 keV, the energy from 90-degree scatter.

Table 5-2. Attenuation in aluminum phantom

Position in Phantom	Fraction of Unattenuated Photons (%)
Incident photons after first shell	90 %
Incident photons after second shell	78 %
Incident photons at center of phantom	66 %
Scattered photons from center, to detector	46 %

The table shows that the attenuation is quite extensive. A photon scattering from the center has a significant probability of being attenuated before reaching the detector array. In the image reconstruction, there was not enough energy information to recreate the image. Attenuation is a significant cause of this problem. In order to simulate a clinical measurement, data duplication allowed for simulated detector arrays to be assigned opposite the original array, as shown in Figure 5-3. The data on the phantom is symmetric to allow for this duplication. The duplication of the data produces a clearer image of the entire phantom. Figure 5-3 shows the position of the source-detector-phantom geometry used for the image reconstruction. Each black line represents the location of the detector array relative to the source and phantom. It does not represent a specific amount of data sets.

Although three sets of data were taken for each phantom (position-1, position-2 and position-3, shown in Figure 4-4), only two sets were used in the image reconstruction. A limitation of the reconstruction algorithm did not allow for the data set at position-3 to be included. The images created would improve with the addition of position-3. Therefore, each solid bar depicted in Figure 5-5 represents only position-1 and position-2 data sets.
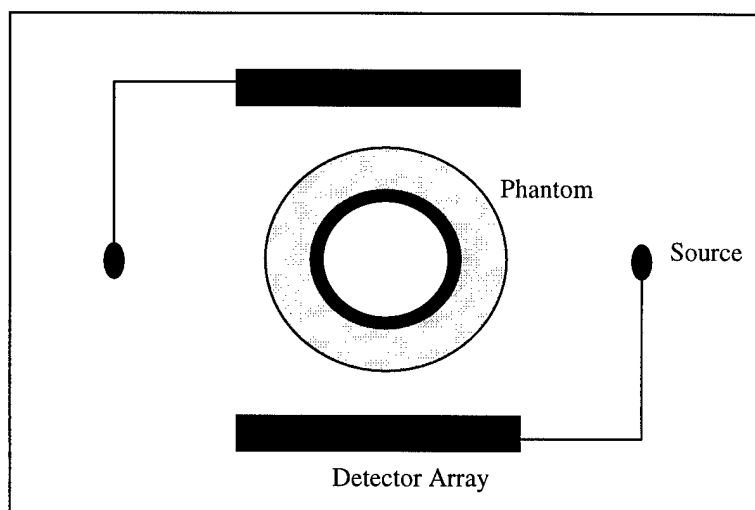
Figure 5-3. The geometry used for image reconstruction. Note that only two source positions are used, with three data sets per source location. Each array contains four detectors.
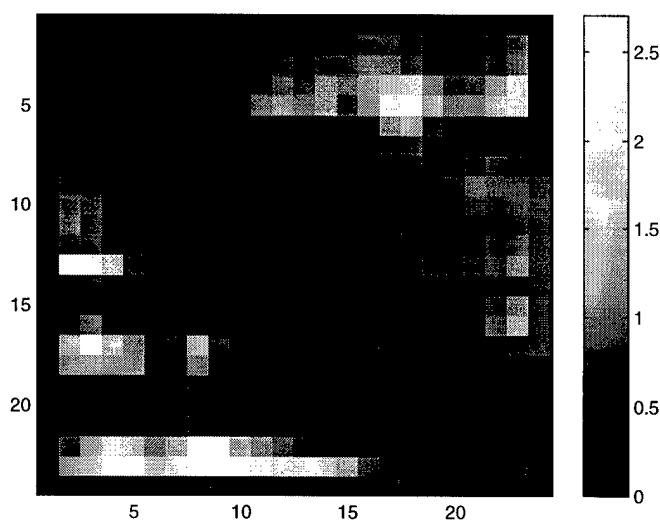
Figure 5-4. An image of MCST data uses six sets of data. The six data sets include position-1, position-2, position-3 and their duplicates. The entire phantom is not resolved. This is due to the attenuation that occurs in the aluminum.

The geometry in Figure 5-3 shows the data duplicated to simulate a source on both sides of the phantom, with detectors on opposite sides. This solution uses all three

positions of data, duplicated for both source positions to provide a better image. However, this duplication did not create a clear image, and additional source-detector positions were required to resolve the phantom image. Figure 5-5 shows the positions of four source locations.
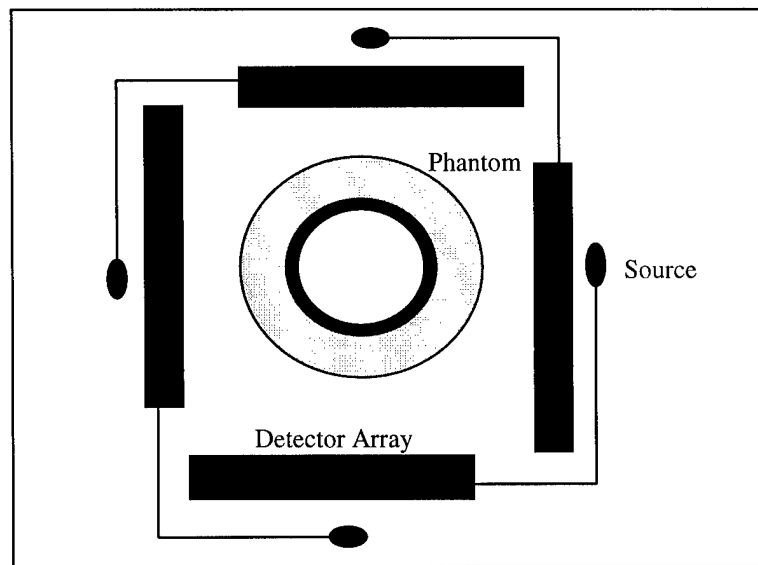
Figure 5-5. The four source location geometry used for image reconstruction. Only two data sets are used per source location, due to a limitation in the image reconstruction algorithm.

Using the geometry in Figure 5-5, images were created from both the simulated spectra and the detector data. The simulated data produces a clearer, more defined image. Since the same Scattergram code is used to simulate the data and calculate A^0 (the initial mapping of electron density to detector signals) the simulated images are expected to be better than measured images. To simulate the actual data, random Poisson noise was added to the simulation data before reconstruction. The model data demonstrates the "ideal" images created by the MCST. Using additional detectors in each array, and amassing a larger data set will cause the detector data to come closer to

the "ideal" modeled data. The following images are from simulated data for all of the cases (thin-void, thin-osteoporotic, thin-normal, and thick-osteoporotic).

Each image used the initial density guess of a normal trabecular bone density from Figure 5-2. Each of the images used a factor of $\beta=5$, $\omega=0.5$ during the image reconstruction with 20 'outer' iterations of A.

(a)

(b)

(c)

(d)
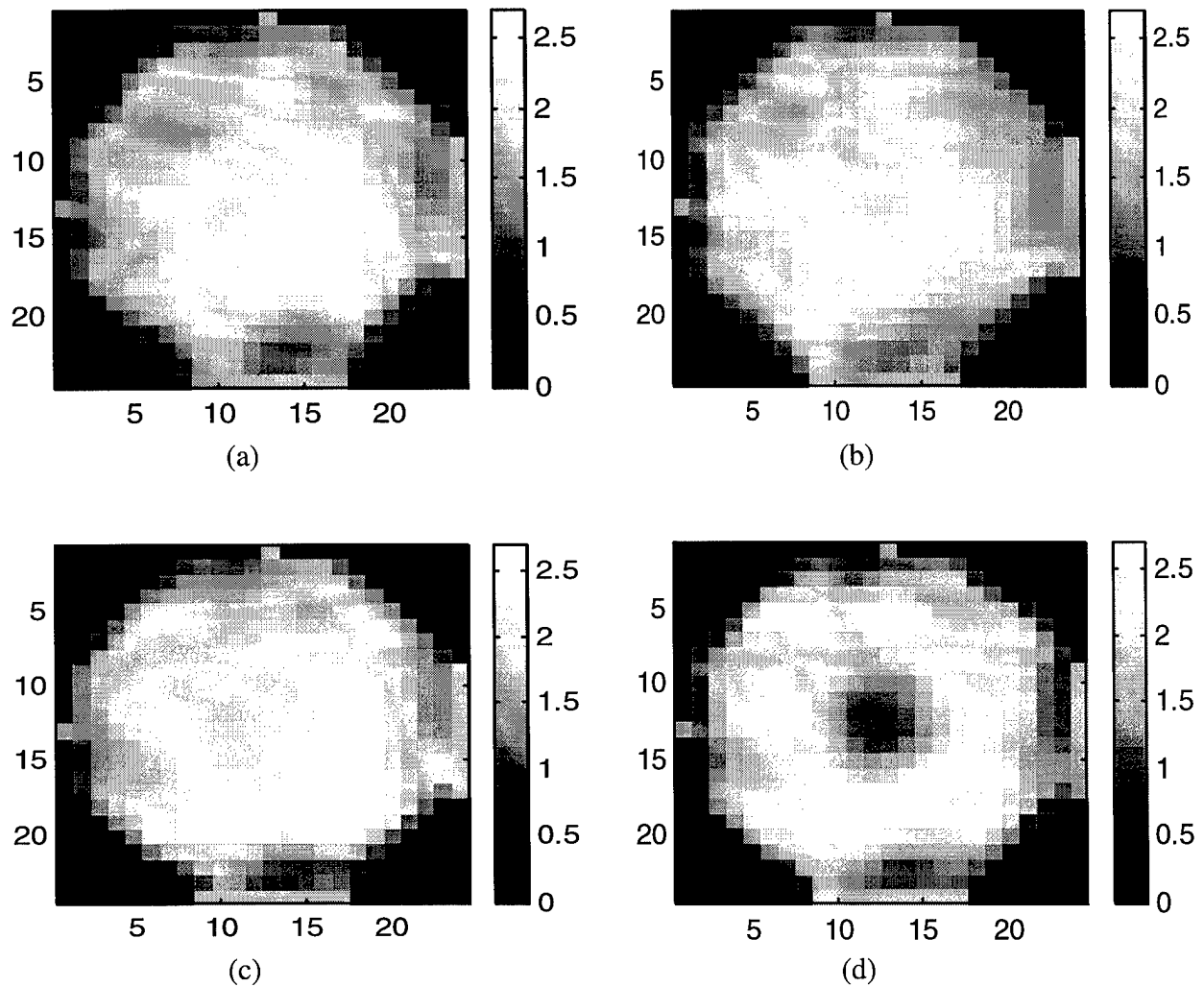
Figure 5-6. Reconstruction of the phantom using simulated Scattergram model data. (a) shows the thin cortical shell with a normal trabecular density (Thin-Normal). The additional images are (b) Thick-Osteoporotic, (c) Thin-Osteoporotic, (d) Thin-Void.

Displaying a vertical slice through the center of each image and plotting them together gives a relative density for each of the phantoms shown in Figure 5-6. As seen in this plot (Figure 5-7), the MCST was able to differentiate between the density values. The simulated images were created in the same manner of data duplication as the detector data. Each data set was a re-arrangement of two data sets (position-1 and position-2). This was done so a correlation in noise was present in all cases for true comparison.
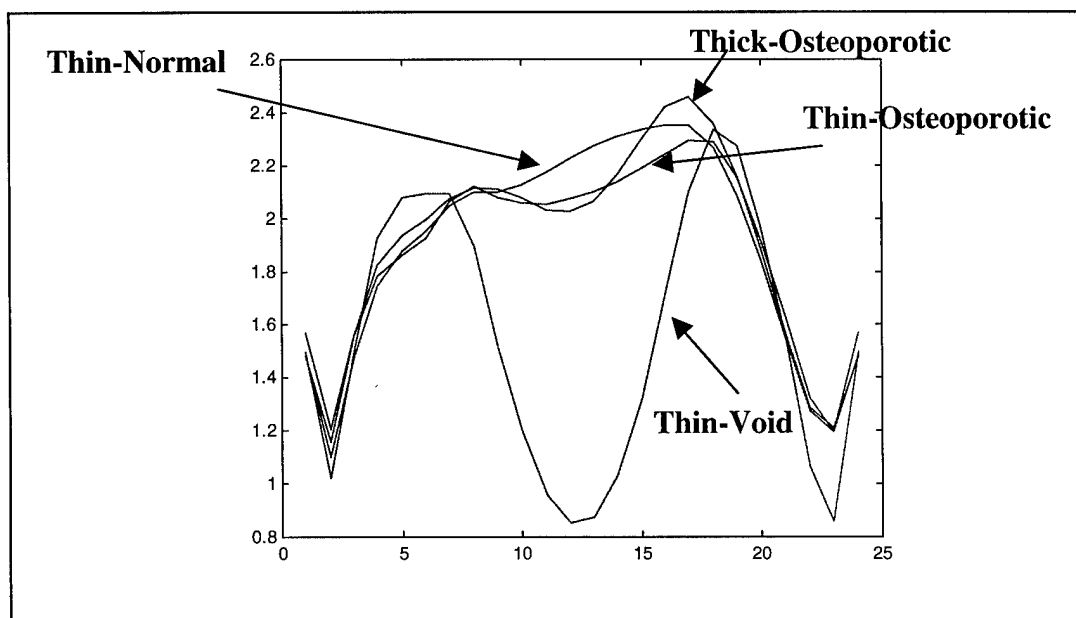
Figure 5-7. A vertical slice through the center of all four images. The thick-osteoporotic density increases slightly at the cortical layer compared to the thin-osteoporotic density. Note that both of the osteoporotic densities are close, despite the higher attenuation due to the thicker cortical shell.

The reconstructed images from the detector data are shown in Figure 5-8. These images again show a variation in the trabecular density. Each image used a value of $\beta=1$, $\omega=0.5$ during the image reconstruction with 20 outer iterations of A.
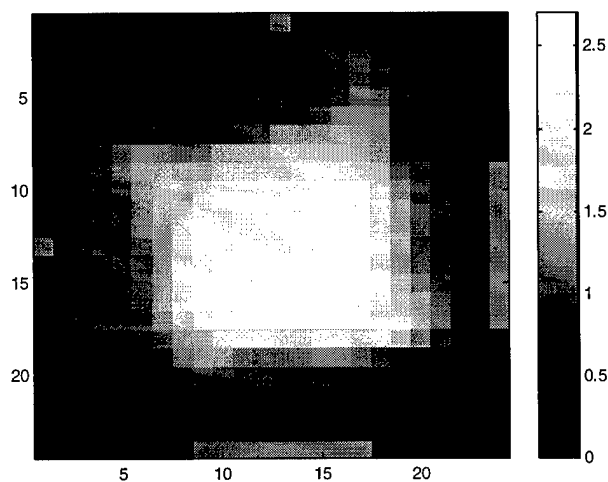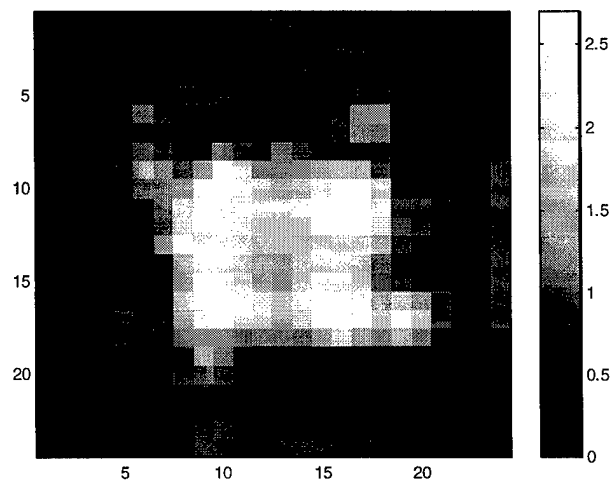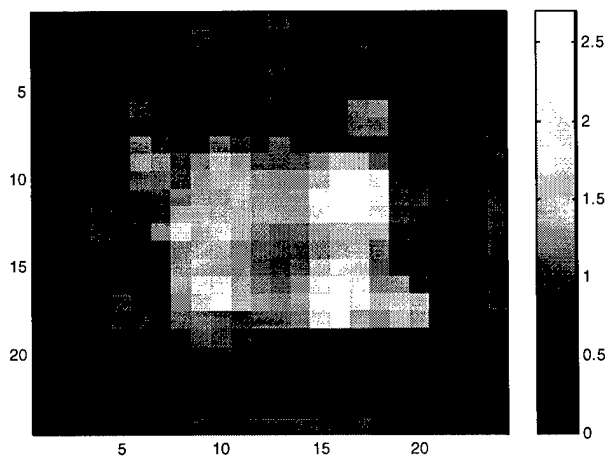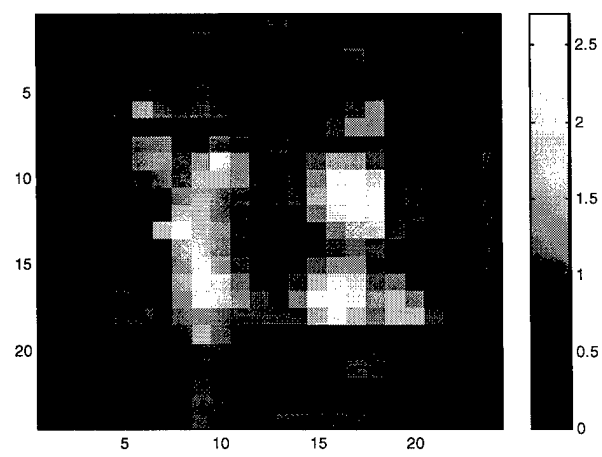
Figure 5-8. Reconstruction of the phantom using detector data. (a) shows the thin cortical shell with a normal trabecular density (Thin-Normal). The additional images are (b) Thick-Osteoporotic, (c) Thin-Osteoporotic, (d) Thin-Void.

The vertical slice was again taken for each image and used for comparison, shown in Figure 5-9.
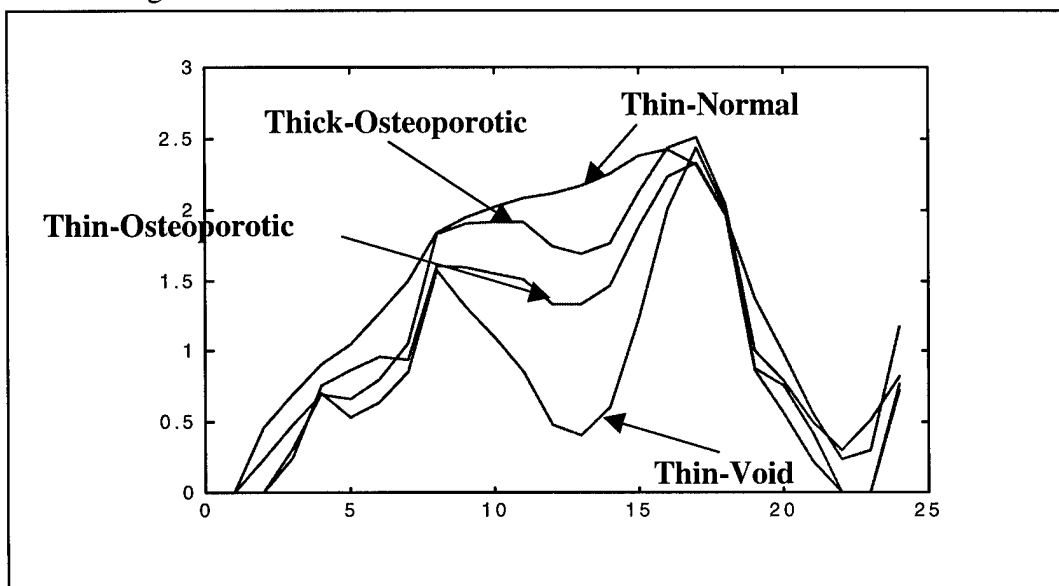
Figure 5-9. A slice through the center of all four phantoms. Again, distinctions can be made between each of the phantoms.

Impact of Duplicating Data

In the Scattergram simulation, each detector had its individual set of noise data added to the data set. However, when reconstructing the images from the detector data, each data set is copied (both signal and noise). This causes a correlation in the noise between different sets of data. Due to this, using multiple detectors in multiple locations is essential to reproducing an image of a bone phantom. The resulting images were obtained by using only position-1 and position-2 data sets in the four-source location geometry due to a limitation in the image reconstruction algorithm.

Each of the images using the MCST data sets has a substantial decrease in quality from the simulated data sets. This decrease in image quality can be partially attributed to the amount of noise modeled, drift of calibration data, and multiple scattering contributions. These factors all played a part in the final image quality. However, despite these issues, the images were distinct enough to identify which of the relative levels of trabecular density was used.

Simulation of Improved MCST

The MCST detector array has a field of view limitation due to the distance the germanium crystal is set back from the detector window as discussed in Chapter III, shown in Figure 5-10 (A). The Scattergram code was used to determine the quality of the image if the crystal was placed flush with the window, as shown in Figure 5-10 (B).
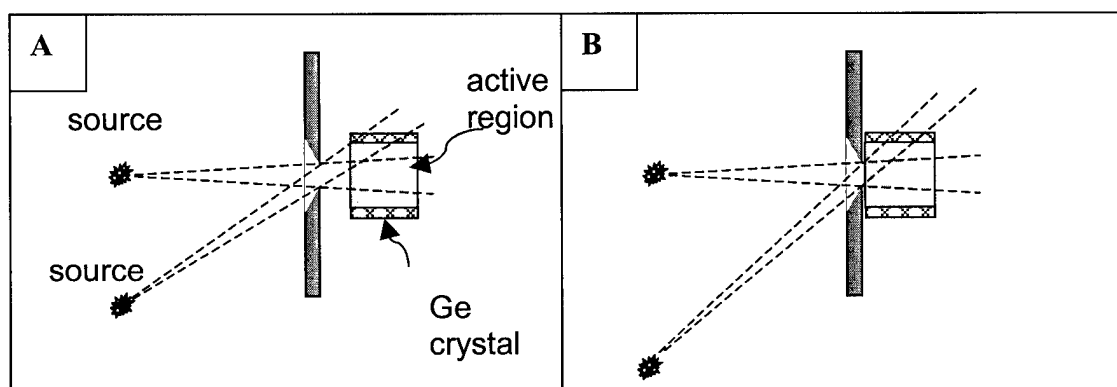
Figure 5-10. Improved MCST design. This improvement moves the detector crystal forward against the detector aperture. The result increases the detector field of view. (Provided by B.L. Evans)

The Scattergram code simulated the impact of this change. All other variables remained the same, i.e. the duplication of the data, geometry of phantom and correction

polynomial. The images were expected to be a higher quality base on the increased amount of angular information gained. Due to the higher incident angles that can be detected per crystal, previously lost information is retained in the new design. The images in Figure 5-11 are the result. The vertical slice was taken through the center of each image and compared against improved phantoms simulated, shown in Figure 5-12.
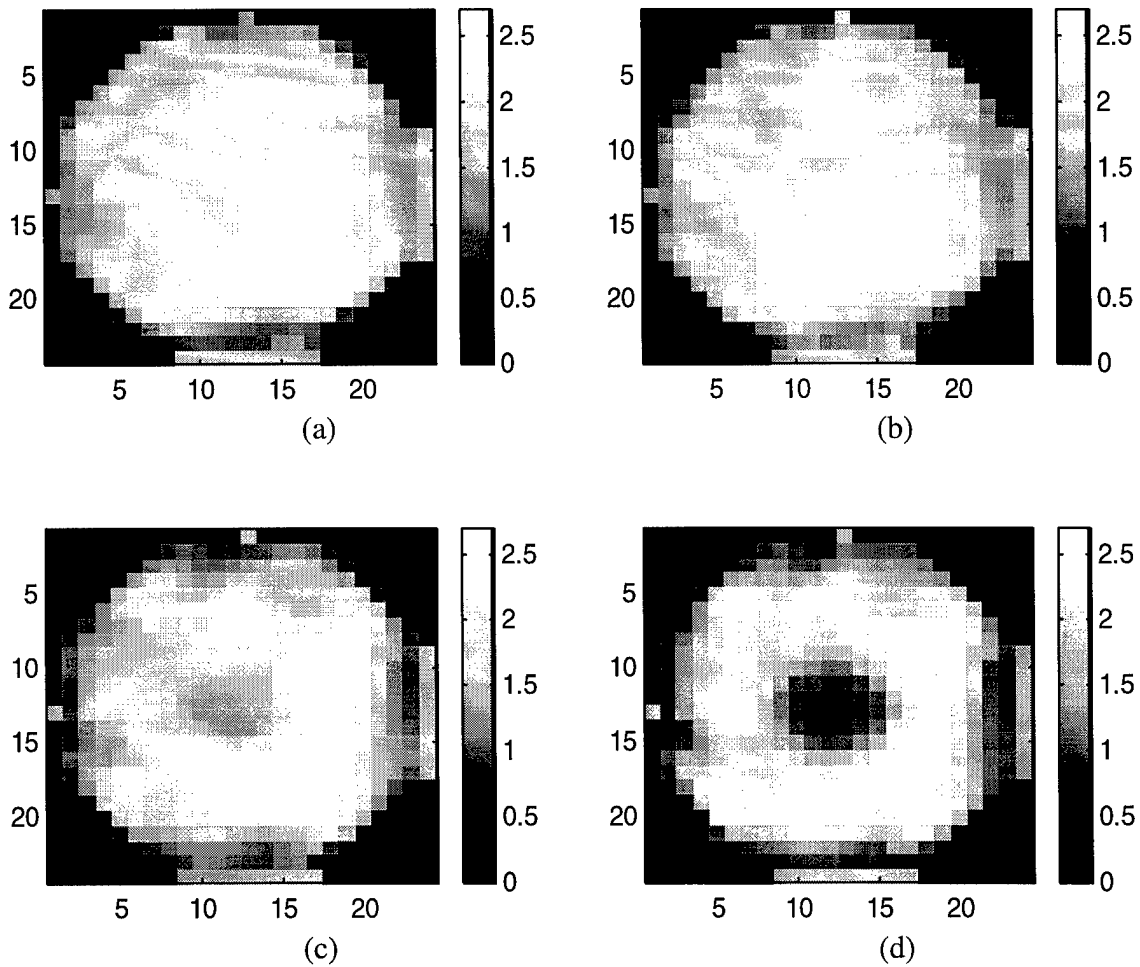
Figure 5-11. Images using the improved MCST simulation data. (a) Thin-Normal, (b) Thick-Osteoporotic, (c) Thin-Osteoporotic, (d) Thin-Void.
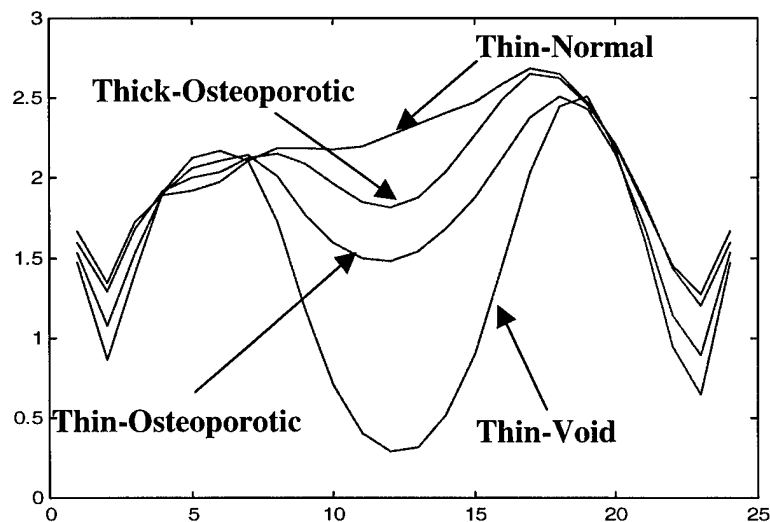
Figure 5-12. A vertical slice through the center of all four of the improved MCST images.

Image Comparison

The images were compared in order to quantify the image quality. Table 5-3 compares the values of image intensity of the trabecular density. Since the soft tissue was not designed properly in the phantom, the comparisons are all relative to the value of the normal trabecular density.

Table 5-3. Comparison of densities relative to value of normal density in the trabecular volume. All values were taken from the reconstructed images.

Source of Data	Osteoporotic Density (thick shell)	Osteoporotic Density (thin shell)	Void Density
Actual Phantom	60 %	60 %	0 %
Data Images	78 %	62 %	13 %
Model Images	92 %	89 %	38 %
Improved Images	80 %	66 %	11 %

Table 5-3 shows interesting results. The improved model and the detector data images compare very well. Both sets of comparisons are much closer to the actual values than the modeled data images. At this time, the problem with the model has not been determined.

Another method of relative comparison can be in image differencing. Figure 5-13 shows the results of modeled images subtracted from each other.

(a)

(b)

(c)

(d)
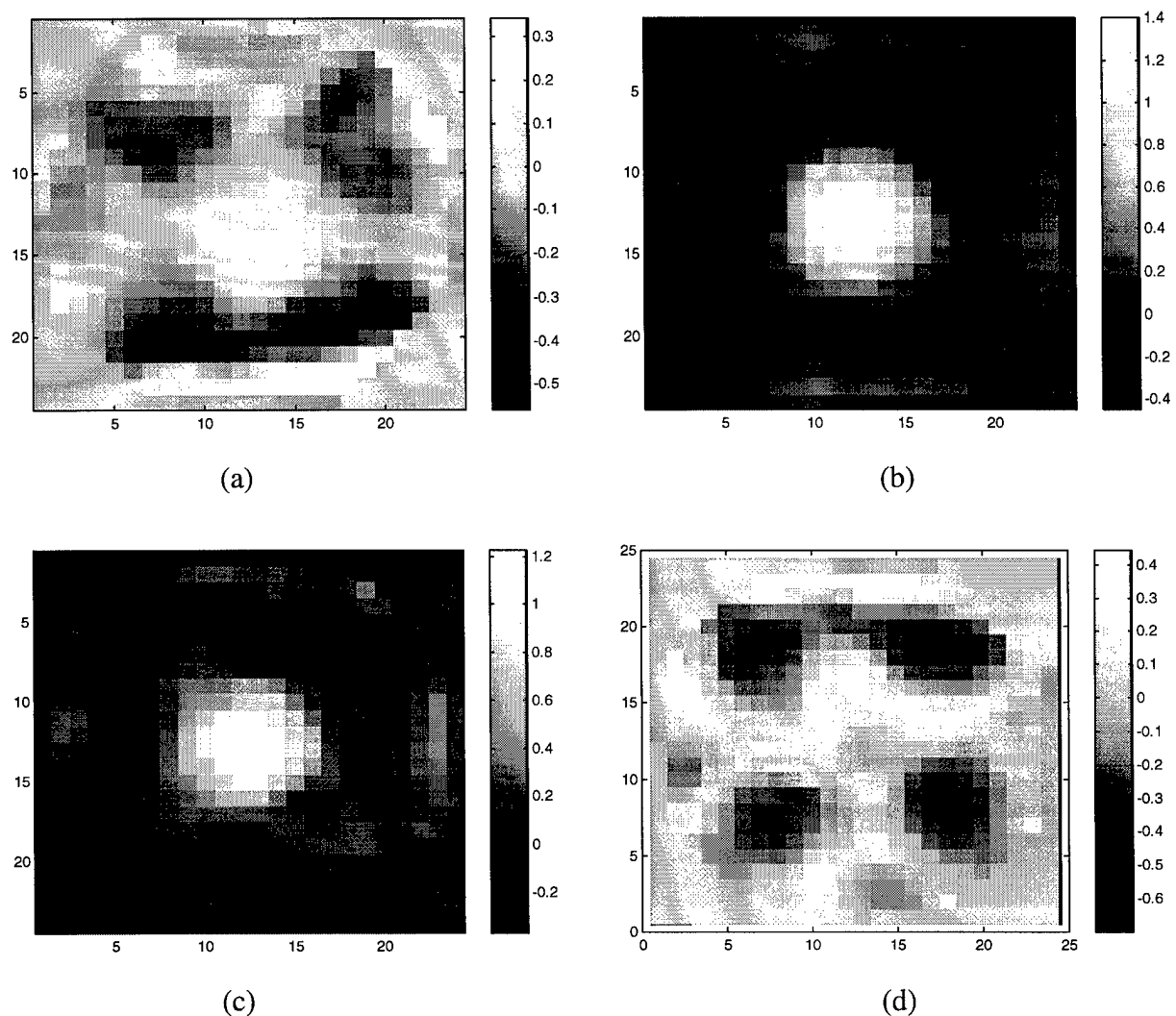
Figure 5-13. Image subtraction of model. The simulated images are (a) Thin-Normal minus the Thin-Osteoporotic, (b) Thin-Normal minus the Thin-Void, (c) Thin-Osteoporotic minus the Thin-Void, and (d) Thick-Osteoporotic minus the Thin-Osteoporotic.

Image subtraction allows a location and extent of variations to be quantified. This is important for the medical application where time history imaging could provide useful information on the depletion of bone. Figure 5-14 shows the image differences for the detector data. Figure 5-15 is the same comparison of the improved MCST images using simulated data.
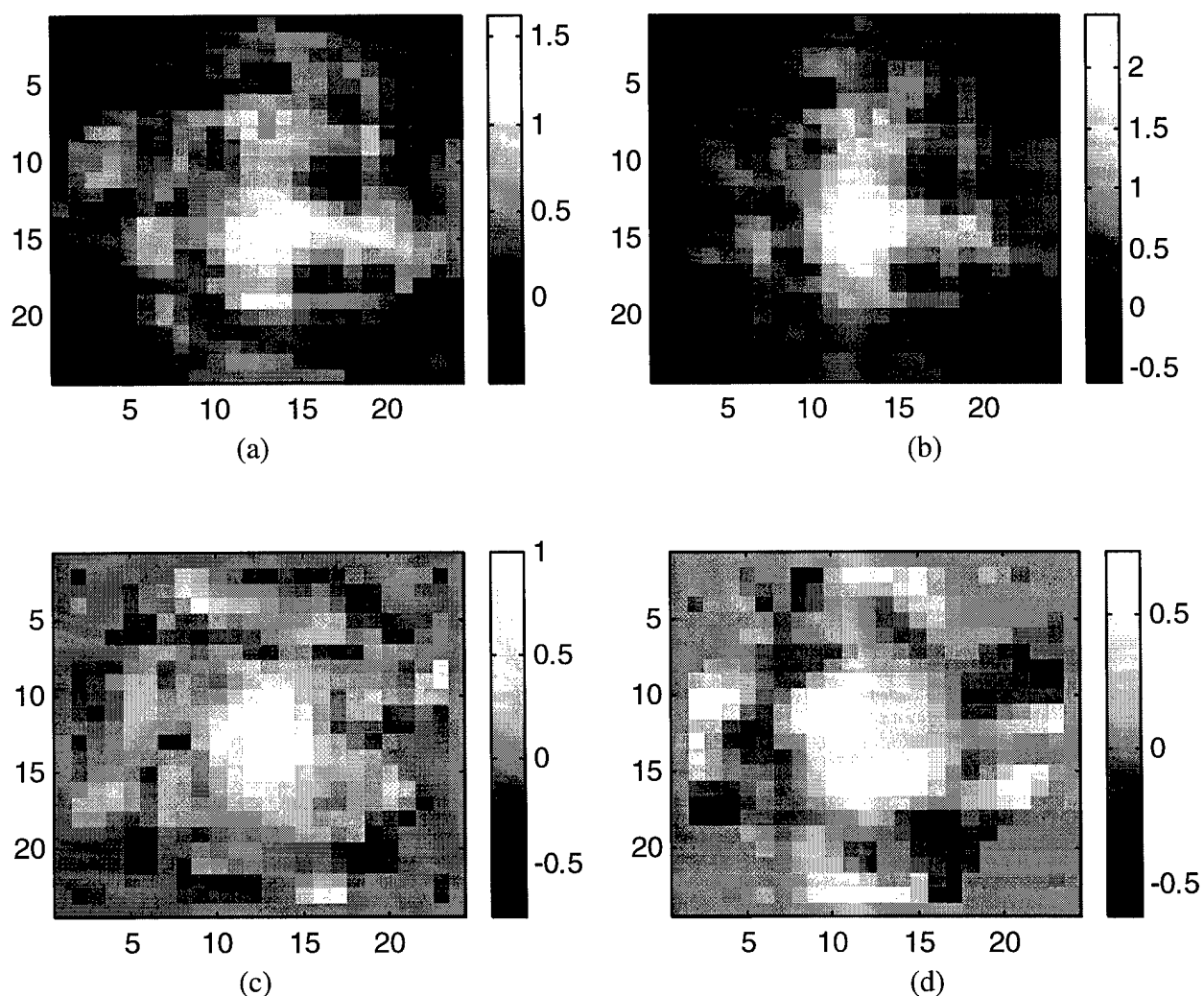
Figure 5-14. Image subtraction of detector data. The images are (a) Thin-Normal minus Thin-Osteoporotic, (b) Thin-Normal minus Thin-Void, (c) Thin-Osteoporotic minus Thin-Void, and (d) Thick-Osteoporotic minus Thin-Osteoporotic.
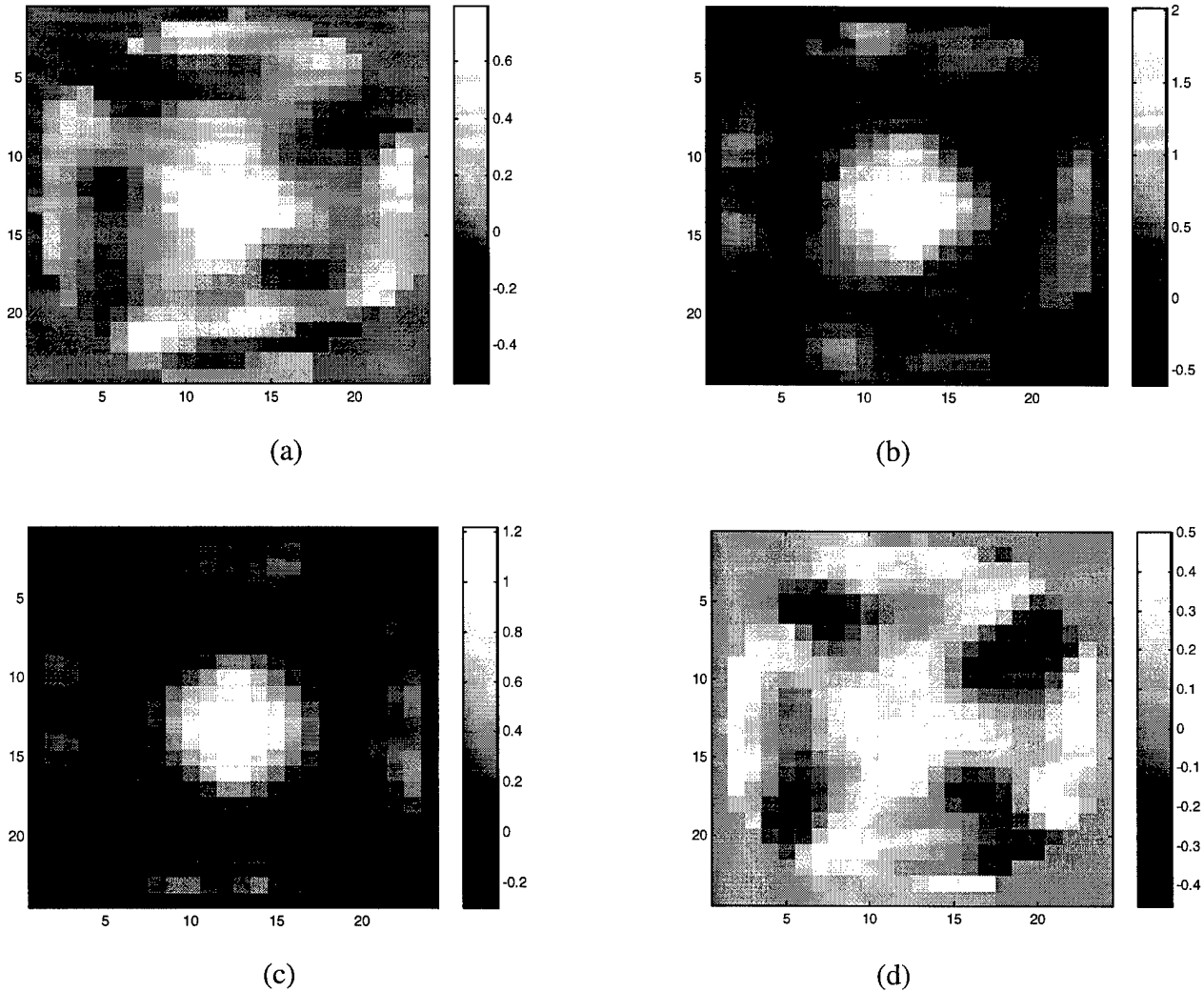
Figure 5-15. Image subtraction of improved MCST model. The simulated images are (a) Thin-Normal minus Thin-Osteoporotic, (b) Thin-Normal minus Thin-Void, (c) Thin-Osteoporotic minus Thin-Void, and (d) Thick-Osteoporotic minus Thin-Osteoporotic.

The subtraction of the images shows distinct locations were the phantom density changed. The magnitude of those changes is reflected in the scale of the images. As seen in both the Scattergram model and the Improved MCST model (Figure 5-13 and 5-14), there is symmetry of the resulting image. This is due to the data duplication that occurred in producing the images. This symmetry is not clear in the detector data.

In all of the images and slices taken of the data, it is clear that distinct differences due to density changes were found.

VI. CONCLUSIONS AND RECOMMENDATIONS

This chapter discussed the overall goal of the project and the extent that the goal was successfully obtained. Some complications developed in completing this project. This chapter addresses those issues with recommendations to the correction action required. Future work in this area is also considered in this chapter with an estimation of the next step in the MCST evolution to monitor osteoporosis.

Overview

This project was designed to investigate the MCST as a potential method for monitoring osteoporosis. The investigation included fabrication and measurement of a bone density phantom. The phantom fabricated represents a single bone surrounded by soft tissue. The phantom is designed to allow changes to the trabecular volume density. The different densities reflect a normal trabecular bone density, an osteoporotic density (60 % of normal), and a void density. A previously developed computational model was used to simulate the recorded energy spectra from the MCST detector array. The simulated spectra were compared against the measured data spectra. Images were created using both the simulated data and measured data. The reconstructed bone density images from both model and detector data were used to determine the effectiveness of MCST in differentiating between the three densities.

Conclusions

Development of the phantom was not done accurately. However, this inaccuracy does not invalidate this project's results. Although the soft tissue density was created too high, the focus of the project is on the trabecular density region. This project was designed to measure the differences in this region.

Despite these problems, the MCST was able to produce images that identified phantom density differences. The osteoporotic decrease (60% of normal density) was identifiable from the images. This amount of density loss is not physically possible and represents an extreme. Osteoporosis causes a much lower decrease in density. However, this was used to determine the capability of the MCST to discern an extreme case.

Using image subtraction, it was quite apparent where and to what extent the images differed. As expected, the highest differences were between the normal density and the void density. There were also discernible differences between the thick cortical osteoporotic density and the thin cortical osteoporotic density.

Although additional work is required, this project showed the MCST is capable of distinguishing the features represented by the trabecular bone. This was the goal of this project. The positive result warrants further research in this area.

Recommendations for Future Research

The duplication of the data necessary for image reconstruction resulted in a duplication of the noise from the original data set. This caused a correlation in the noise from one set to the other. Collecting more data sets instead of duplicating existing information would alleviate the problem. The unique data sets may improve the images.

The extent of the improvement is unknown. The complete impact of the data duplication was not investigated to completion.

The phantom construction should also be redone to more accurately follow clinical phantoms. The phantom should model soft tissue with water and the normal trabecular densities with Lucite (Plexiglas). Having a more accurate phantom is key to the next study.

Additional work also needs to be done to the Scattergram generation code. The code is currently not able to simulate the Compton broadening that the Lucite will cause. This is not a trivial area of work. However, this would be crucial if using a more accurate phantom. In addition to this, additional work could be done to take into account multiple scattered photons collected.

The detector collimator also could require additional work. A decrease in the collimated fan beam thickness collected by the detector array would reduce multiple scattered photons detected. The source collimator creates a thin fan beam for the incident photons. However, the detector collimator allows a much larger slice thickness to reach the detector array. This permits a higher contamination of multiple scattering events. Using a more restrictive detector collimator would reduce this contamination and result in a higher ratio of single-scatter-to-multiple-scatter photons collected, thus improving the image quality. However, this becomes a mute point if the Scattergram code is modified to account for the multiple scattered photon contribution.

Summary

The investigation into the noninvasive inspection of bone density using MCST proved successful. The current MCST system showed the feasibility of using Compton scattered photons to image loss of bone density simulated with aluminum phantom. Although this is only the initial step in applying MCST to osteoporosis, these results indicate that future research into a MCST system devoted to measuring bone density is warranted.

APPENDIX A: PSF POLYNOMIAL FIT

The polynomial fit was designed to register the imaging region based on measured data from the MCST. A single bar of aluminum was imaged in 9 locations in the imaging region as shown in Figure 4-3. In this image, Position-5 was used as the origin of the imaging region, with a Cartesian coordinate system. All distances used are in centimeters.

A simulation determined the predicted energy spectra of each detector. A scaling factor was applied to each of the simulation runs to compare them against the measured data. If the imaging region gave a uniform response across the image plane, then a single scaling factor would be required for a single scatter location. However, this is not the case, since a different scaling factor was required for each data set. This required an adjustment for the position dependent scaling factor.

The Mathematica code used to determine the polynomial fit is as follows:

PSF Position Data:
xpos={-1.981,0,2.489,-1.981,0,2.489,-1.981,0,2.489};
ypos={2.032,2.032,2.032,0,0,0,-2.1,-2.1,-2.1};

PSF Scaling Value Data:
aoe={1.52,1.54,1.5,1.11,1.41,1.69,1.0,1.51,1.75};

Fitting the Data:
valdata=Table[{xpos[[i]],ypos[[i]],aoe[[i]]},{i,1,9}];

Check of Fit:
$1.41 + 7.46 \times 10^{-3} x - 2.18 \times 10^{-2} x^2 + 2.57 \times 10^{-2} x^3 +$
$8.84 \times 10^{-4} y - 4.61 \times 10^{-2} xy + 7.11 \times 10^{-3} x^2 y + 2.71 \times 10^{-2} y^2 -$
$1.02 \times 10^{-2} xy^2 - 2.81 \times 10^{-3} x^2 y^2 + 1.92 \times 10^{-3} y^3$

Error=Table[{i,val[[i]]-funcfit[xpos[[i]],ypos[[i]]]},{i,1,9}];
Error//TableForm

Point	Error
1	-8.4376 x 10-15
2	5.3290 x 10-15
3	-4.2188 x 10-15
4	3.3306 x 10-15
5	1.1102 x 10-15
6	-2.2204 x 10-15
7	-8.8817 x 10-15
8	-3.9968 x 10-15
9	6.2172 x 10-15

Physical Plot of the Polynomial Fit:
sur=Plot3D[funcfit[x,y],{x,-2.1,2.1},{y,-2.1,2.1}];
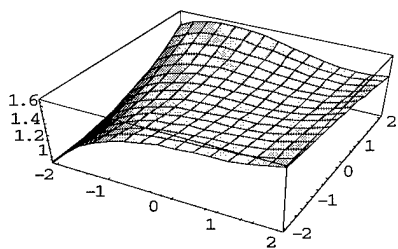
Scatter Plot of the Points:
pts=ScatterPlot3D[valdata,PlotStyle->PointSize[.02]];
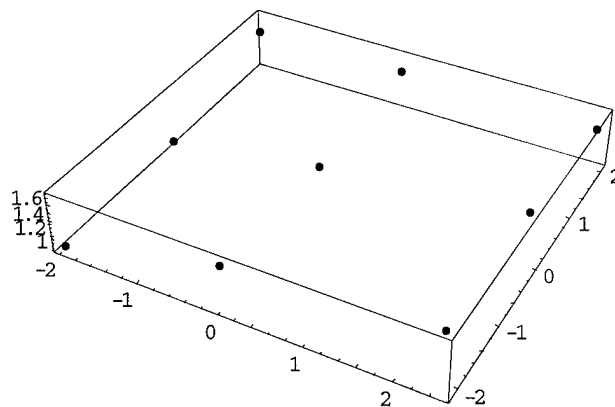
Surface Plot of the fit and the PSF scaling points:
Show[sur,pts];
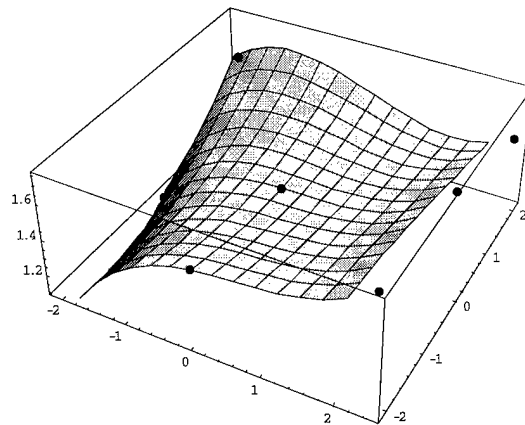
Contour Plot of the Polynomial Fit:

Test[x_]:=RGBColor[x,.25+.75x,.5+.5x];
con=ContourPlot[funcfit[x,y],{x,-2.1,2.1},{y,.1,2.1}, Contours-
>{1,1.05,1.1,1.15,1.2,1.3,1.4,1.5,1.6,1.7} ,ColorFunction->Test];
ShowLegend[con,{Test[1-#]&,8,"1.7","1"}];
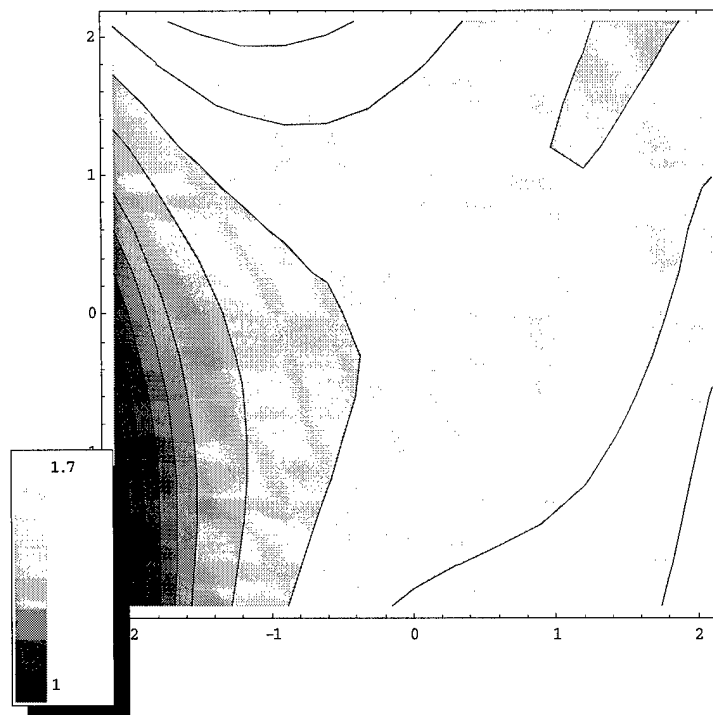
APPENDIX B: ENERGY DATA OF PHANTOMS

Appendix B contains all of the collected data from the two positions used in the image reconstruction. The detector of each position, separated by phantom type, is shown. For comparison, the model (symbols) for each detector is shown with the data. The data has background subtracted from it.
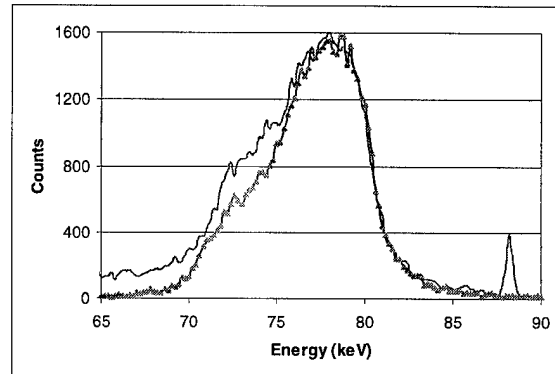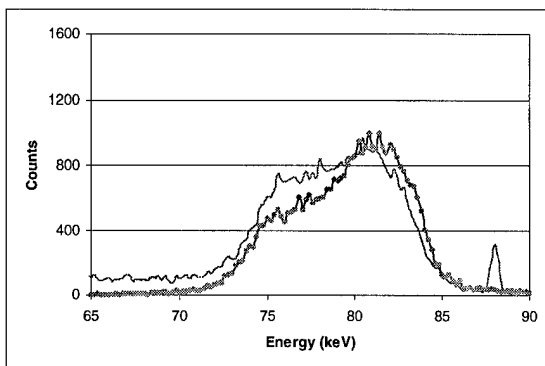
Thin-Normal Phantom: Position 1
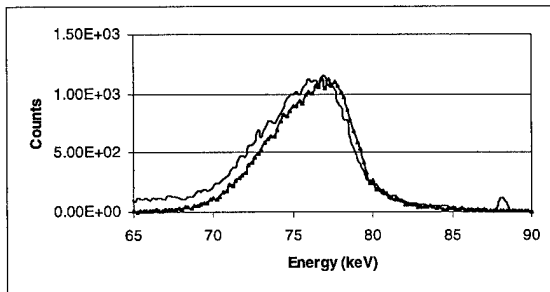
Detector 3
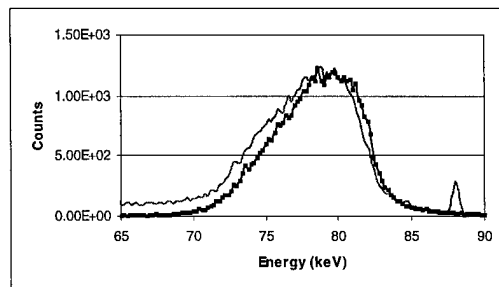
Detector 4
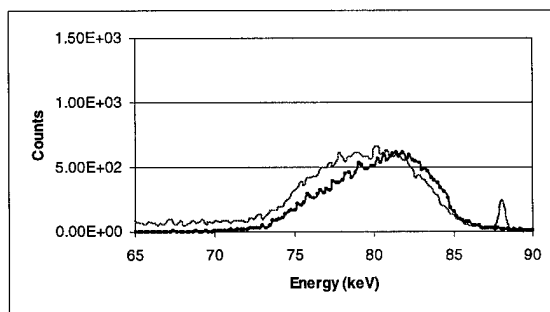
Detector 5
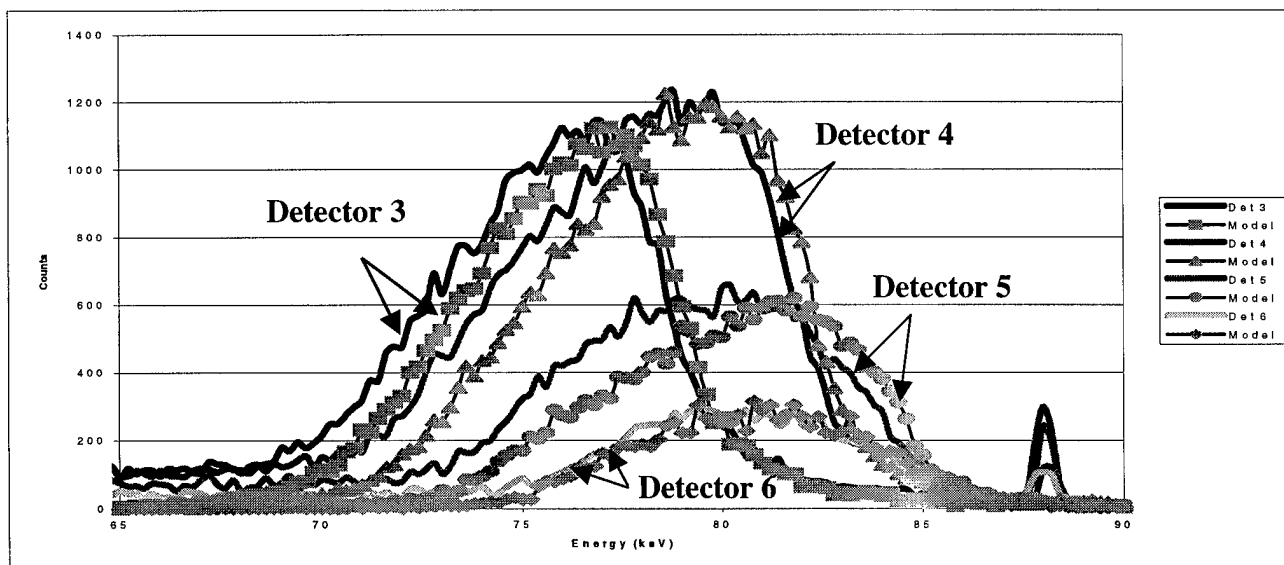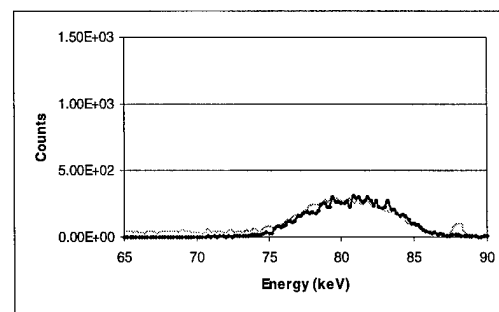
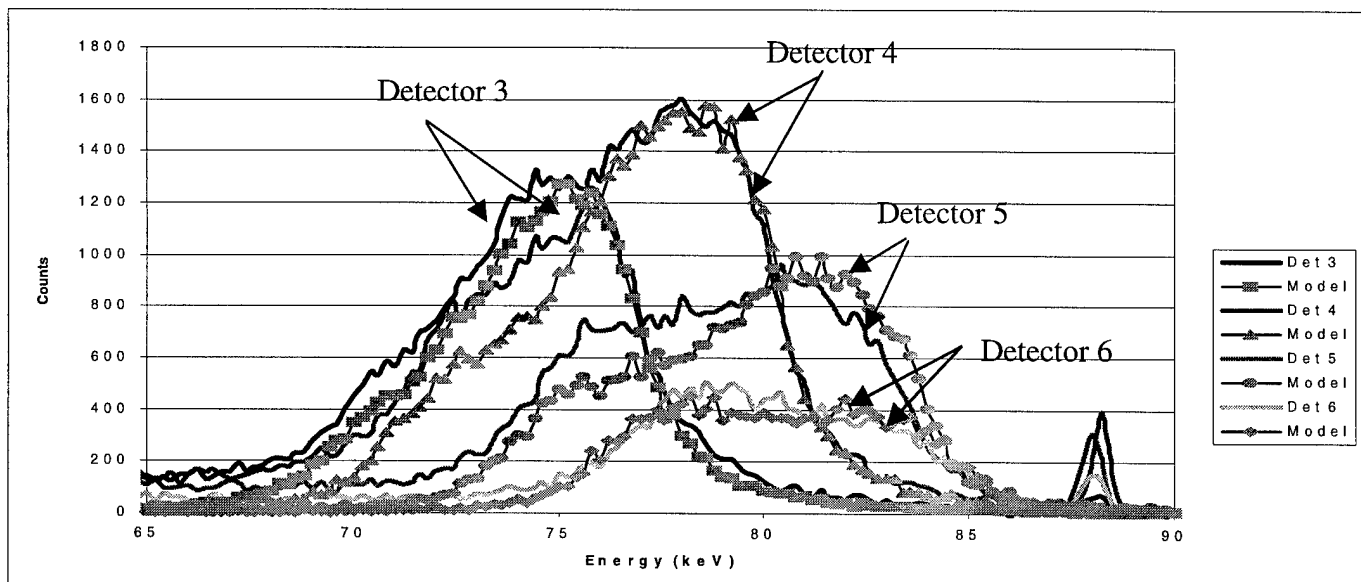Detector 6

Thin-Normal Phantom: Position 2
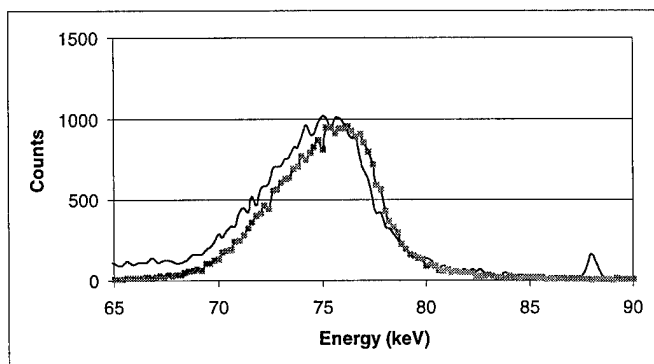
Detector 3
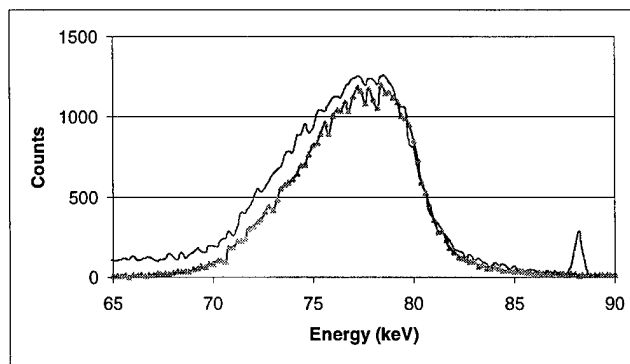
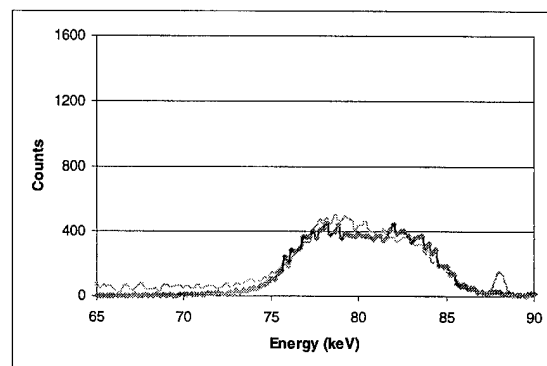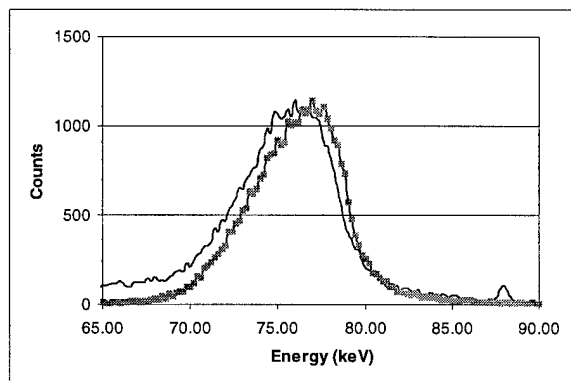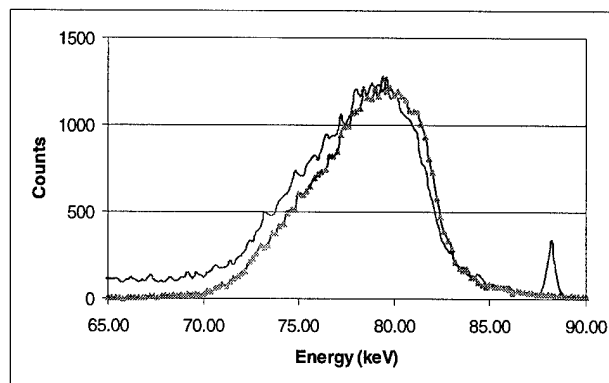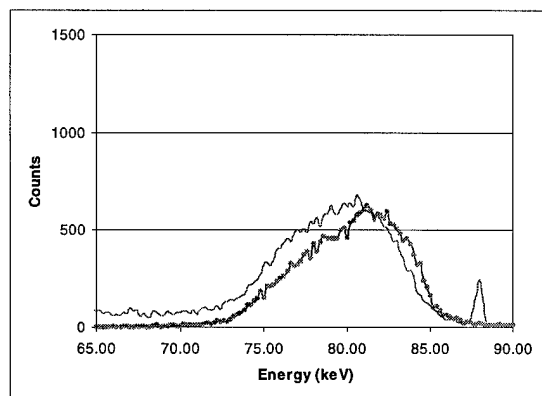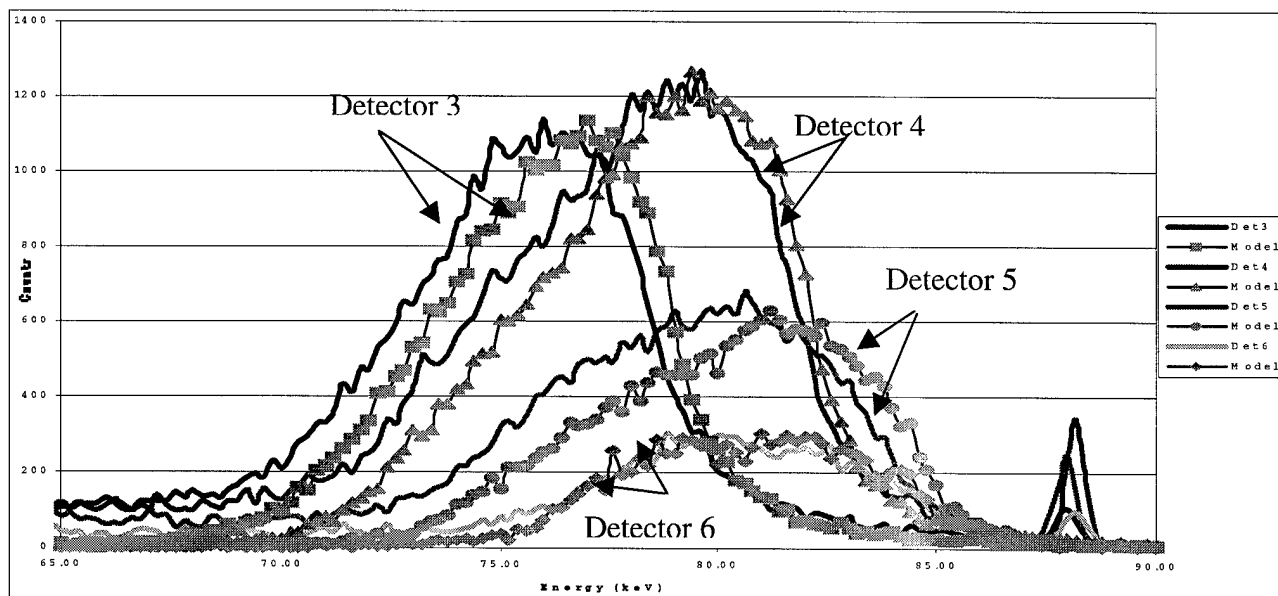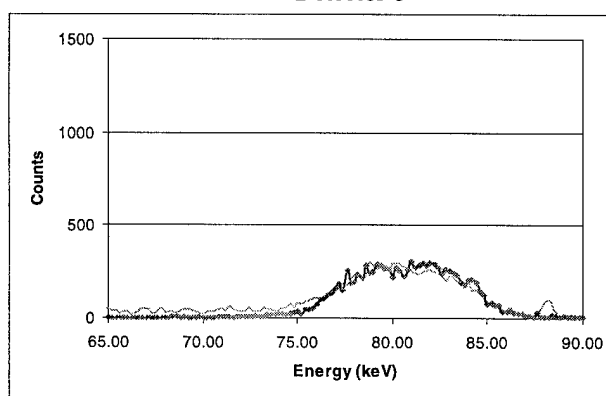Detector 4
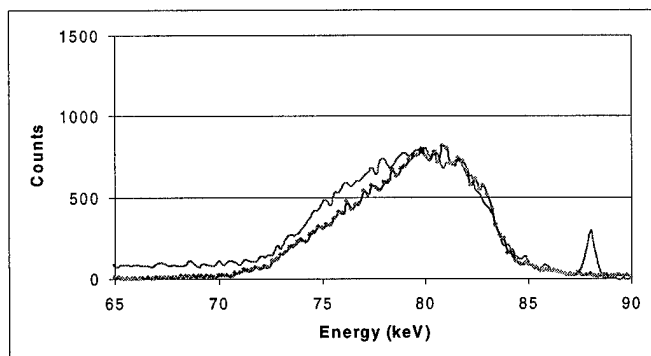
Detector 5
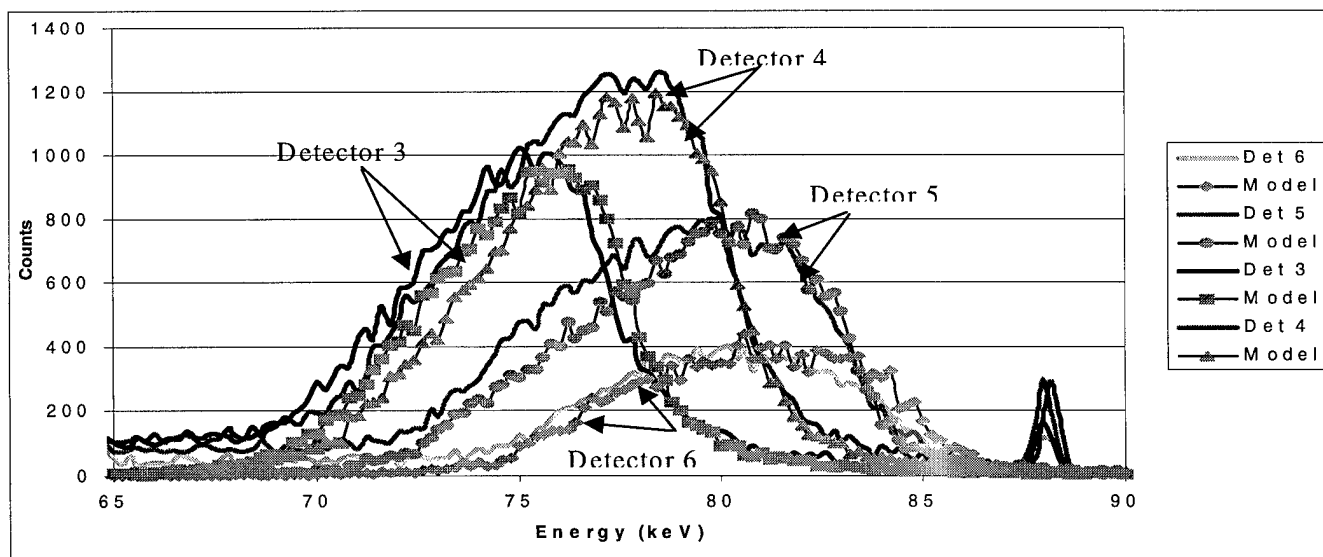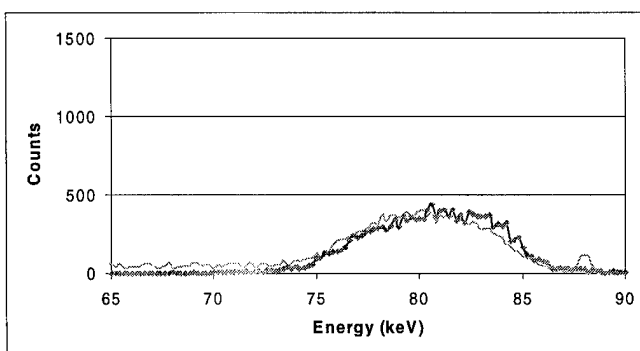
Detector 6

Thin-Osteoporotic Phantom: Position 1
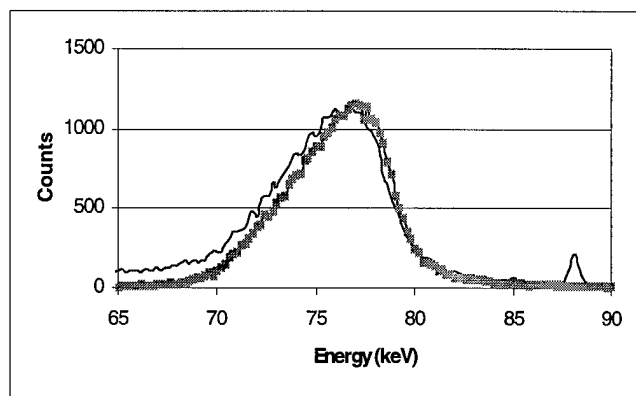
Detector 3
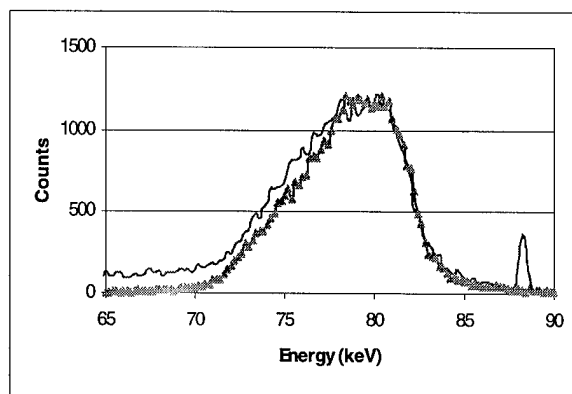
Detector 4
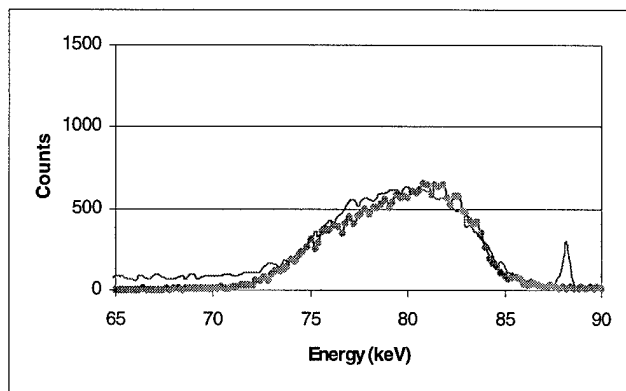
Detector 5

1

Detector 6
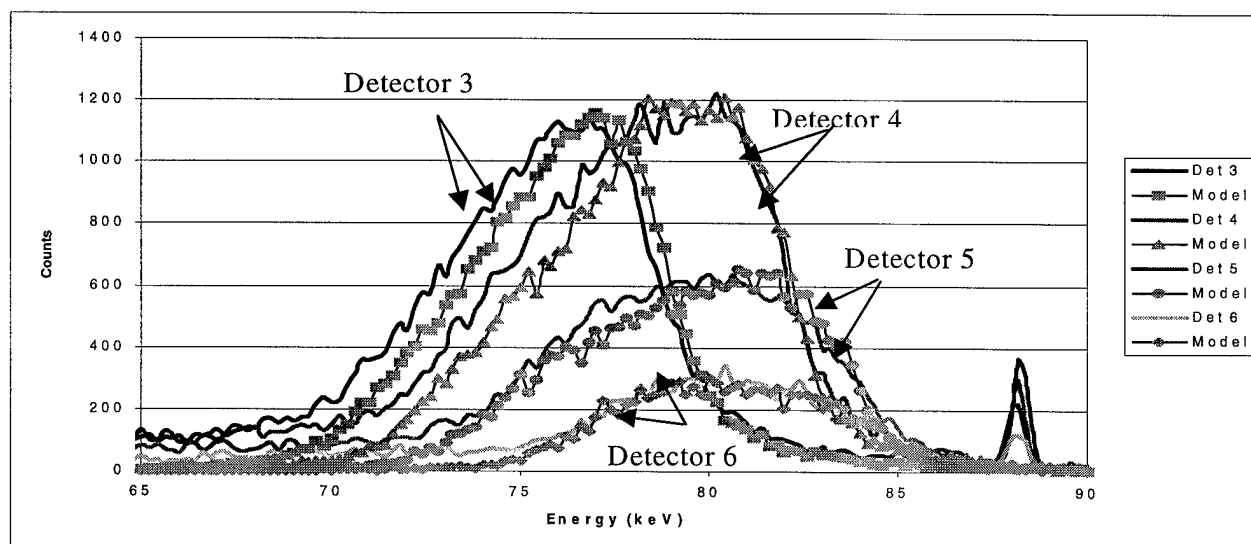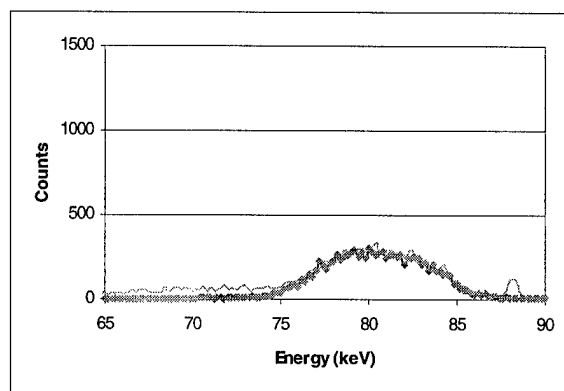
Thin-Osteoporotic Phantom: Position 2
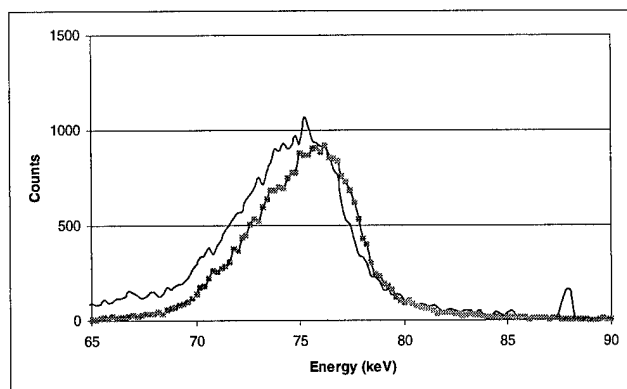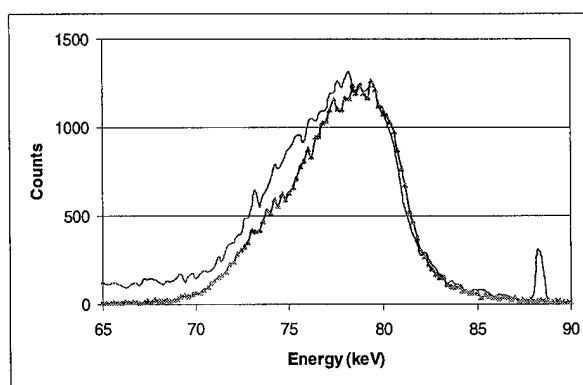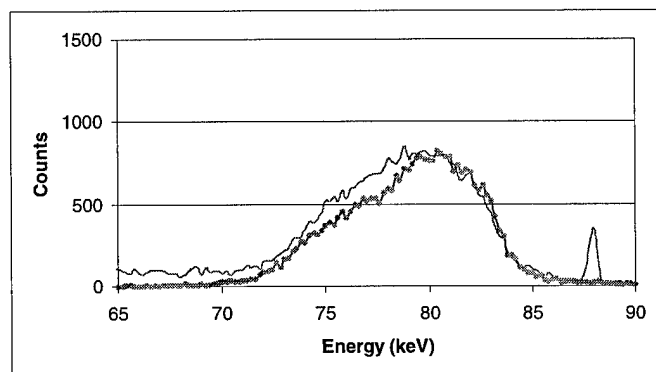
Detector 3

Detector 4

Detector 5
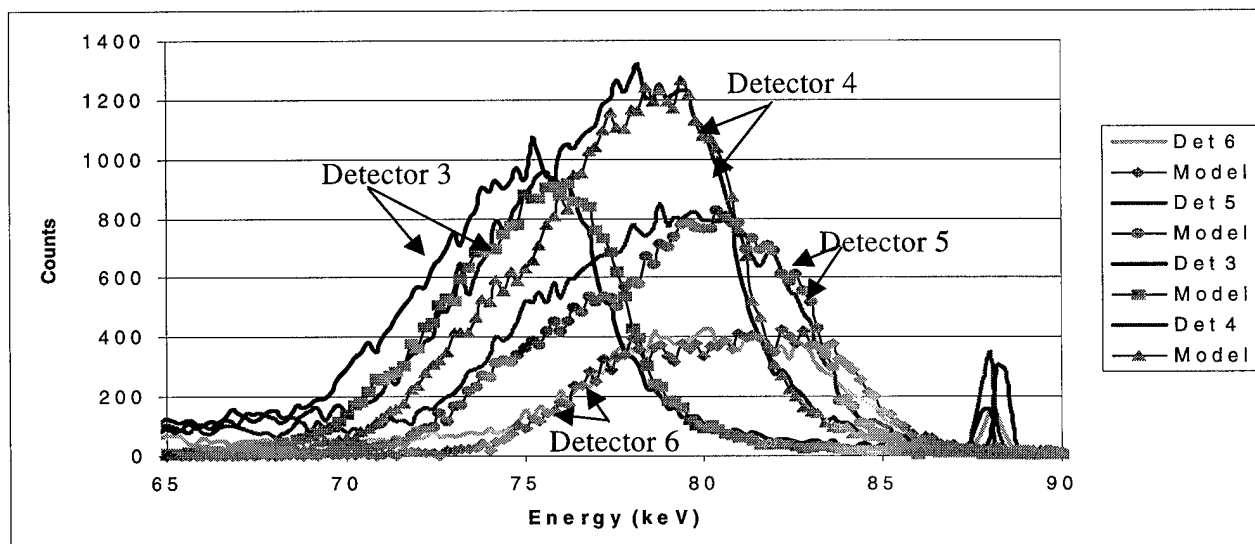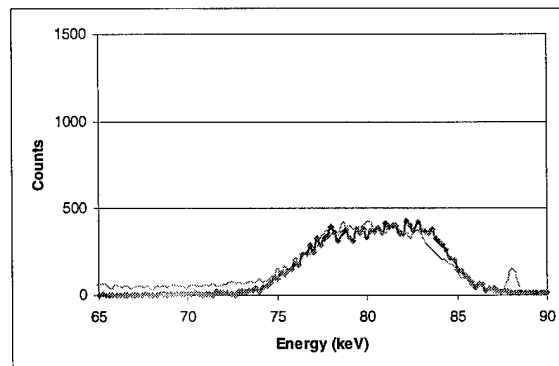
Detector 6

Thin – Void Phantom: Position 1
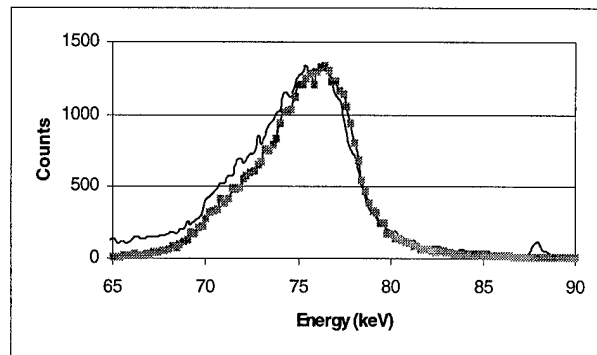
Detector 3
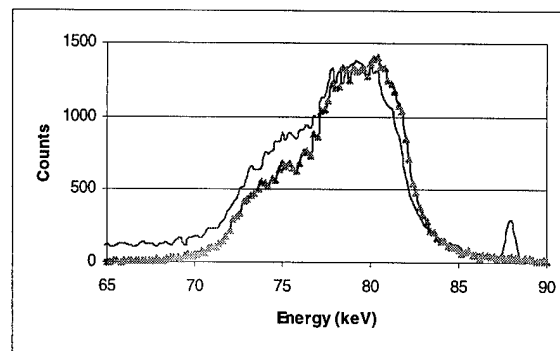
Detector 4
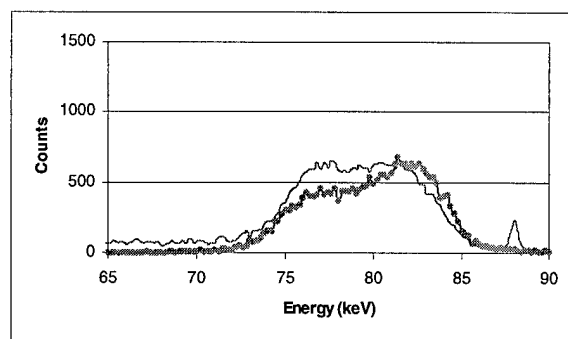
Detector 5
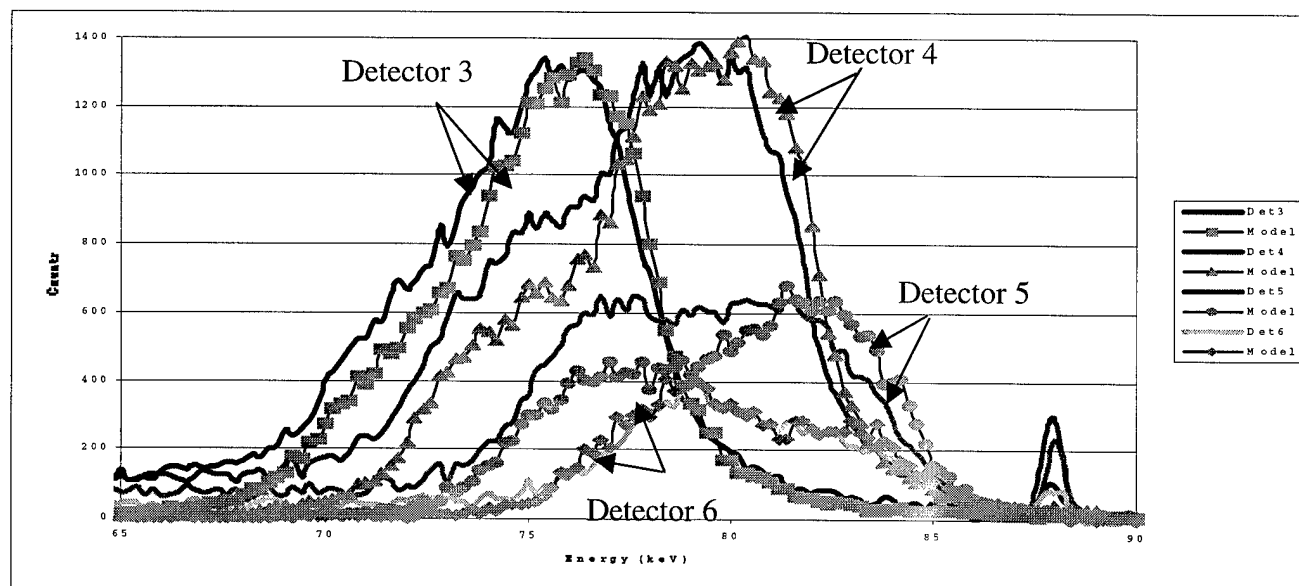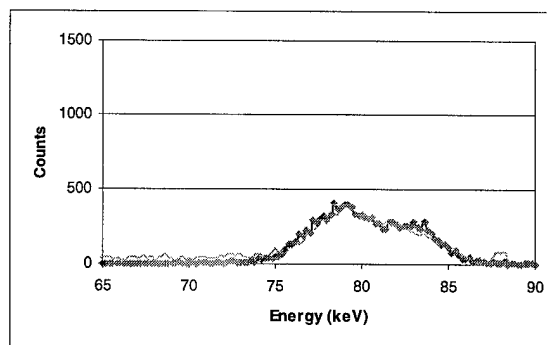
Detector 6

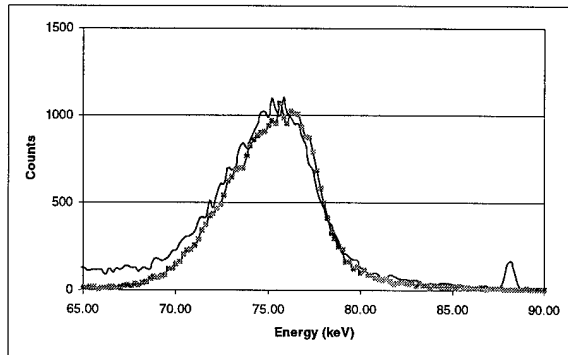# Thin – Void Phantom: Position 2
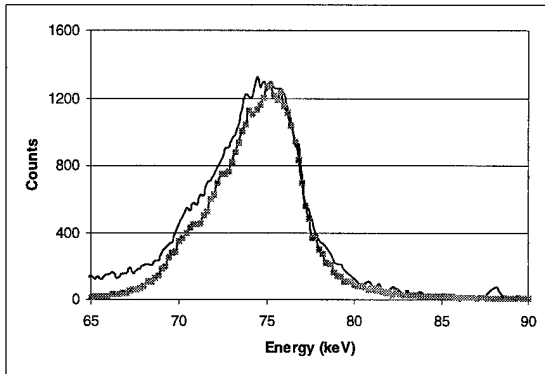
Detector 3

Detector 4

Detector 5

Detector 6

Thick-Osteoporotic Phantom: Position 1

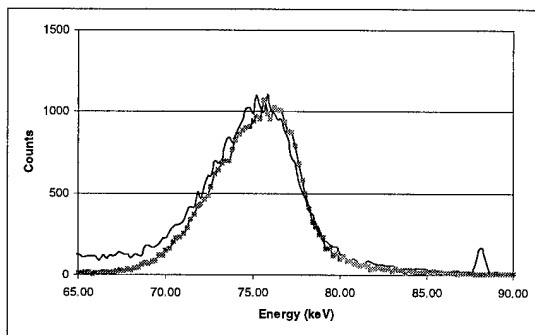## Thick-Osteoporotic Phantom: Position 2
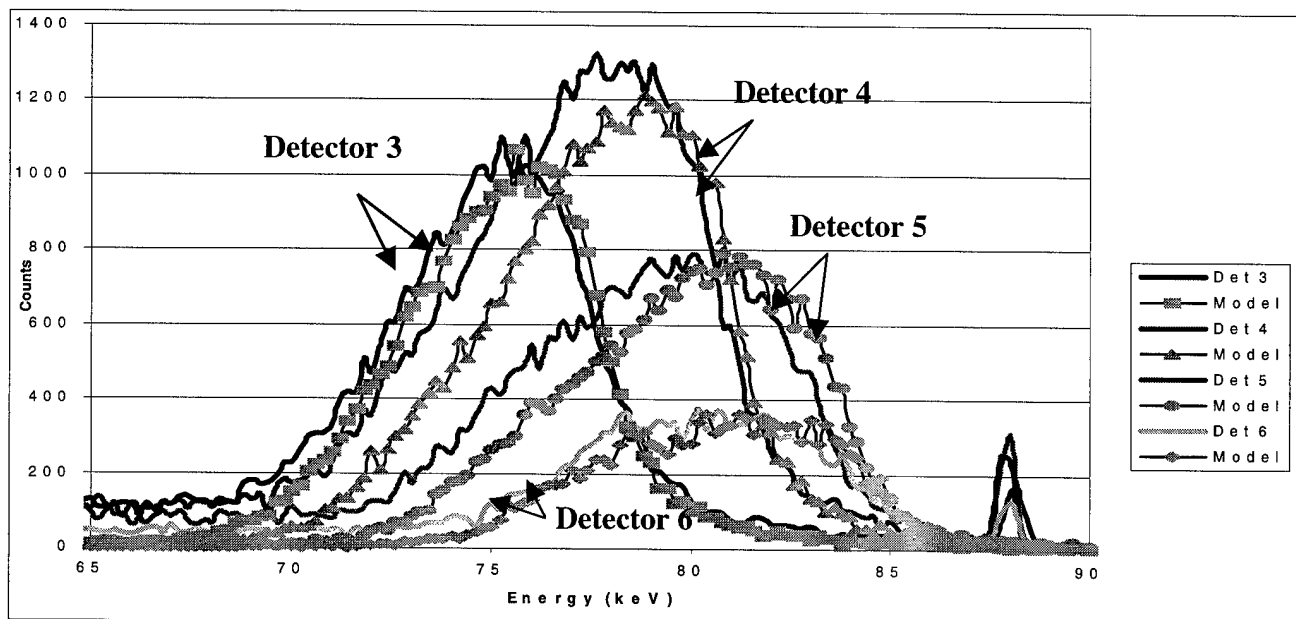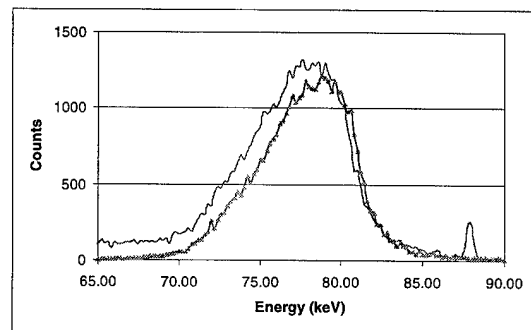
Detector 3
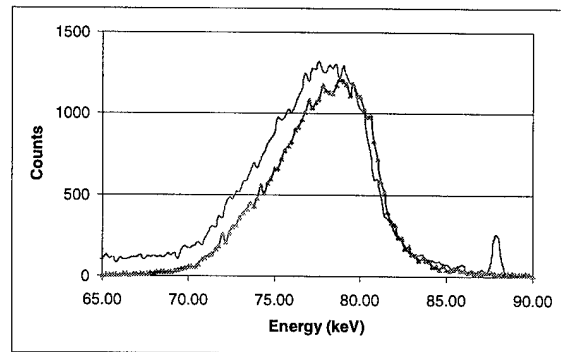
Detector 4

Detector 5

Detector 6

APPENDIX C: PHANTOM DESIGN

The schematic drawings of the phantom are shown in this appendix. The phantom was built by the machine shop located in Building 470. The following are the schematic designs given to the machinists.

Plexiglas for the stand was chosen based on it inexpensive cost, lightweight, and its simplicity to machining. Any material would have done adequately since it is not in the fan beam of the source gamma rays. Figure C-1 shows the design for the stand. The purpose of the stand was to align the center of the phantom with the fan beam source and the detector array.
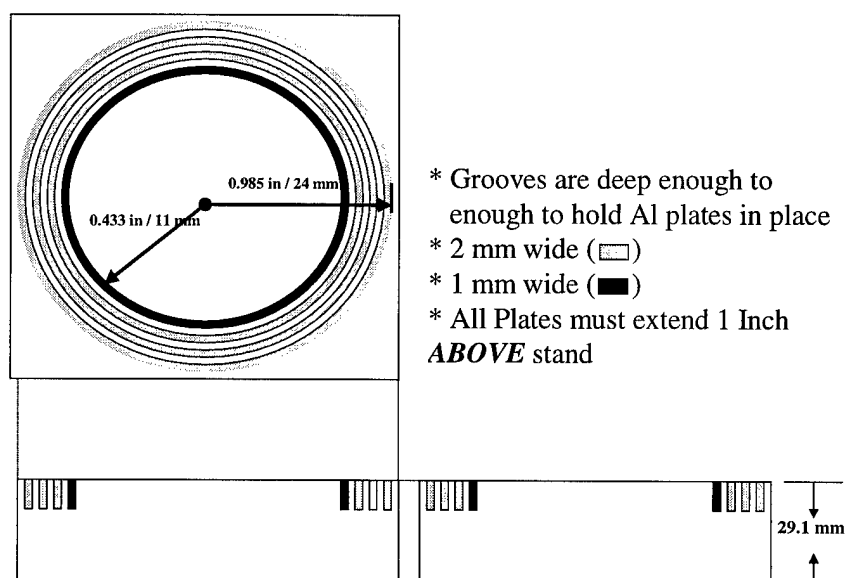

Figure C-1. Plexiglas stand design. This stand holds the aluminum rings in place.

The cortical shells and the soft tissue region of the phantom were machined from pure aluminum. Figure C-2 and C-3 show these shells.

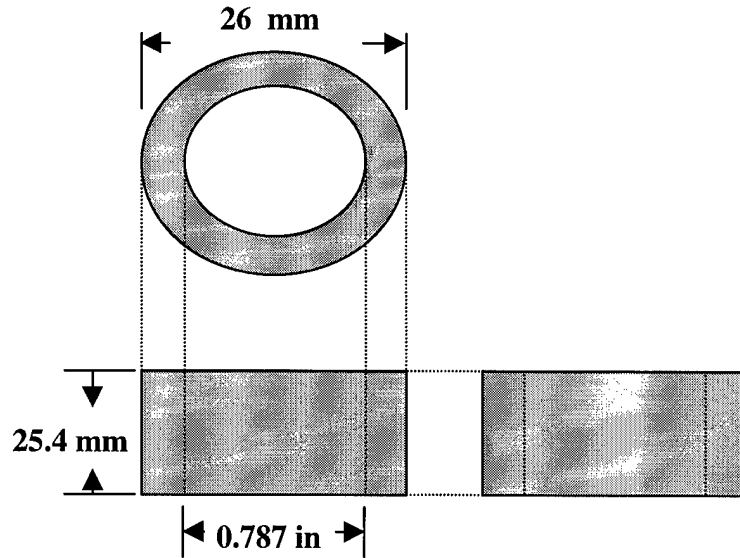Figure C-2. Thick cortical shell design. The aluminum used for the shell is alloy 1100. The aluminum was supplied by the machine shop at AFIT.
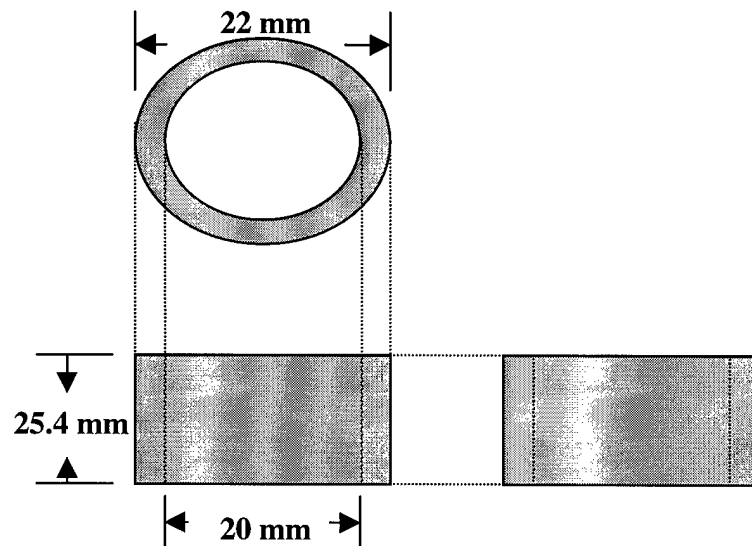
Figure C-3. Thin cortical shell design. The 1100 alloy aluminum is also used for this shell.

The inner shell diameters for both the thick and the thin cortical bone are intentionally the same. This allows the ability to use the same soft tissue region for both shells.

The soft tissue was designed following Figure C-3. The soft tissue shown reflects too high of a density region. This region should be approximately 1.0 g/cm^3, but actually is 1.3 g/ cm^3.

Aluminum Plates - 2 mm thick (▭)
Aluminum Plate - 1 mm thick (▬)
Spacing Between - 2 mm (▭)

* Height of 25.4mm is
ABOVE stand height
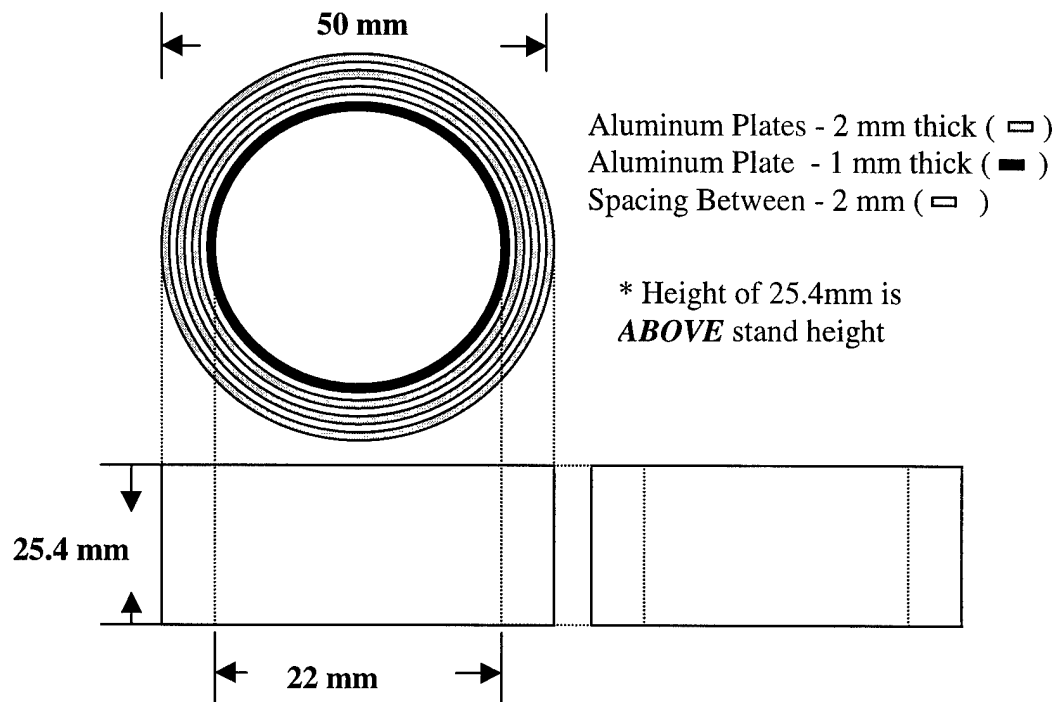
Figure C-3. The soft tissue design. This region calculates a density of 1.3 g/ cm^3.

The schematic drawings of the collimator are shown in the following appendix. The collimator was built by the machine shop located in Building 470. The following are the schematic designs given to the machinists.

TOP
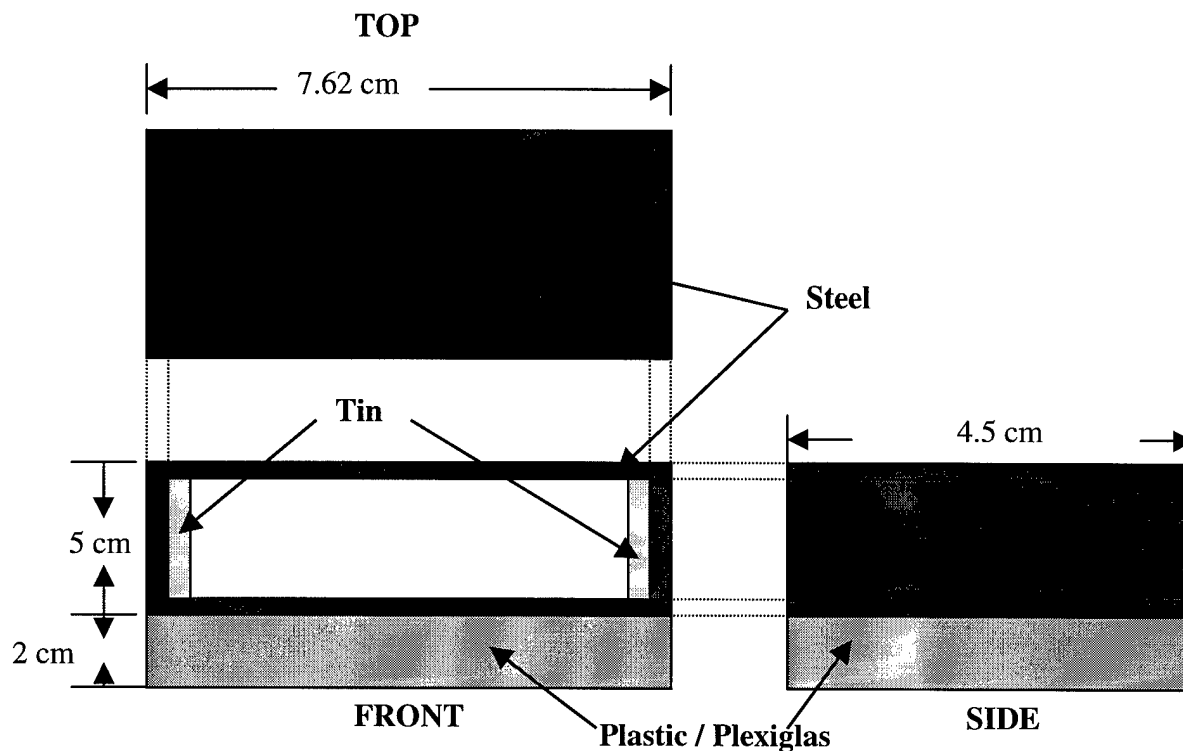
Figure D-1. Collimator Base. This is the first pieces constructed.

The next drawing, Figure D-2, of the collimator are placed on the front and back of the collimator. These tin sheets provide the mask that will only allow a thin (2mm) fan beam of incident photons through the collimator.

TOP

7.62 cm

2 mm

FRONT

SIDE

Figure D-2. Tin mask on collimator base. This mask will absorb the incident photons and only allow a thin beam to pass unattenuated.

TOP

FRONT   **SIDE**

Figure D-3. Complete collimator. This is how the final collimator will look.

BIBLIOGRAPHY

Arendtsz, N.V. and M.A. Hussein. "Electron Density Tomography with Compton Scattered Radiation", <u>Mathematical Methods in Medical Imaging II</u>. SPIE Vol. 2035 (1983).

Barzel US: <u>Osteoporosis II: An Overview</u>. New York, Grune & Stratton, 1978.
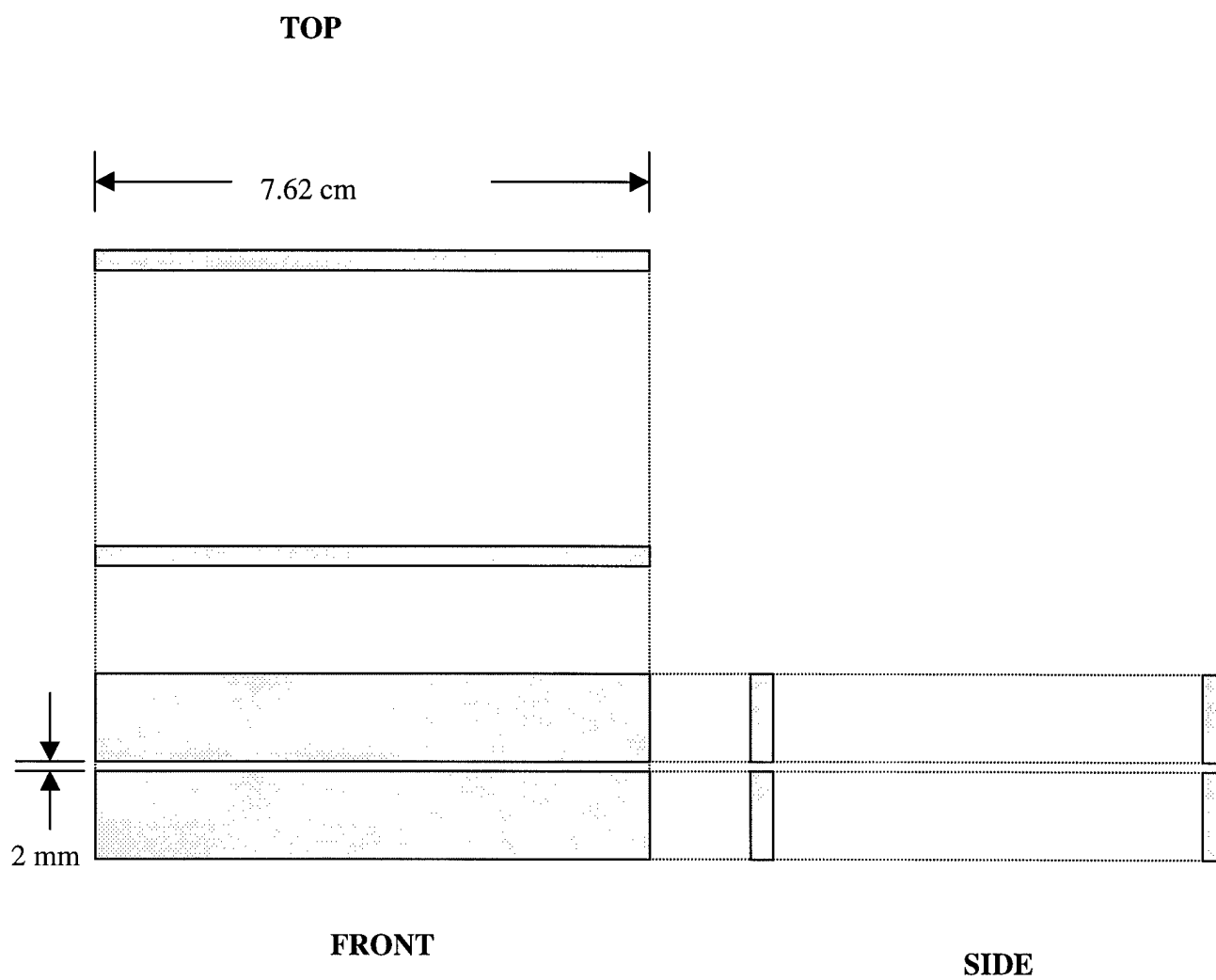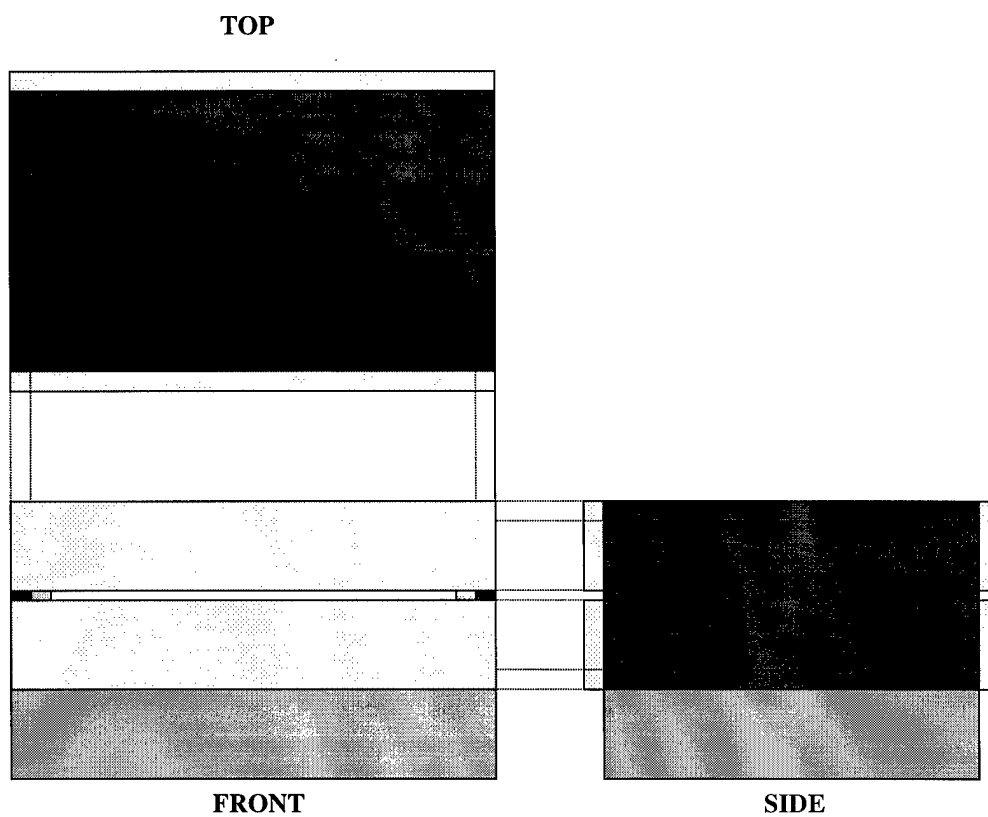
Battista, J. J. and M. J. Bronskill. "Compton Scatter Imaging of Transverse Sections: An Overall Appraisal And Evaluation for Radiotherapy Planning", <u>Phys. Med. Biol</u>. Vol. 26, 81-99 (1981).

Black, J. M. and E. Matassarin-Jacobs. <u>Medical-Surgical Nursing, A Psychophysiologic Approach</u>. Fourth Edition. W.B. Saunders Company, 1993. 1902-1905, 1879-1880.

Cesareo, R., A.L. Hanson, G.E. Gigante, L.J. Pedraza, and S.Q.G. Mahtaboally. "Interaction of keV Photons with Matter and New Applications". <u>Physics Reports</u>. Vol. 213, No. 3., 117-118, (1992)

Cho, Zang-Hee, Joie P. Jones, and Manbir Singh. <u>Foundations of Medical Imaging.</u> John Wiley & Sons, Inc. New York, NY, 1993. 148-152.

Evans, Brian L. Personal Interview. 1998.

Evans, Brian L. "Fan-Beam Multiplexed Compton Scatter Tomography for Single-Sided Noninvasive Inspection". Dissertation. 1999.

Evans, B.L., J.B. Martin and M.C. Roggemann. "Devconvolution of Shift-Variant Broadening for Compton Scatter Imaging". 1998.

Felsteiner, J.R. Fox and S. Kahane. "The Electron Momentum Density in Aluminum". <u>Solid State Communications</u>, Vol. 9, 61-63, 1971.

Garnett E.S., T.J. Kennett, D.B. Kenyon and C.E. Webber. <u>Radiology</u>, Vol. 106, 209, (1973).

Hangartner, Thomas N. Personal Interview. 1998.

Hangartner, T.N. " Correction of Scatter in Computed Tomography Images of Bone'. <u>Medical Physics.</u> Vol. 14, No. 3, 335-340, (1987).

Hangartner, T.N. "The OsteoQuant: An Isotope-Based CT Scanner for Precise Measurement of Bone Density". <u>Journal of Computer Assisted Tomography</u>. Vol. 17, No. 5, 798-805 (1993).

Hangartner, T.N., J.J. Battista and T.R. Overton. "Performance Evaluation of Density Measurements of Axial and Peripheral Bone with X-Ray and Gamma-Ray Computed Tomography". Phys. Med. Biol. Vol. 32, No. 11, 1393-1406, (1987).

Hangartner, T.N. and V. Gilsanz. "Evaluation of Cortical Bone by Computed Tomography". J. Bone Miner. Res. Vol. 11, No. 10, 1518-25, (1996).

Hangartner, T.N. and C. Conrad Johnston. "Influence of Fat on Bone Measurements with Dual-Energy Absortiometry". Bone and Mineral. Vol. 9, 71-81, (1990).

Hangartner, T.N. and T.R. Overton. "Quantitative Measurement of Bone Density Using Gamma-Ray Computed Tomography". Journal of Computer Assisted Tomography. Vol. 6, No. 6, 1156-1162 (1982).

Harding, G. "On the Sensitivity and Application Possibilities of a Novel Compton Scatter Imaging System". IEEE Transactions on Nuclear Science, Vol. NS-29, No. 3, (June 1982).

Harding, G. and J. Kosanetzky. "Scattered X-ray Beam Nondestructive Testing". Nuclear Instruments and Methods in Physics Research. Vol. A280, 517-528, (1989).

Heilmann, P., Wuster, Chr., Prolingheuer, Chr., Gotz, M., Ziegler, R. "Measurement of Forearm Bone Mineral Density: Comparison of Precision of Five Different Instruments" . Calcif. Tissue. Int.. Vol. 62, 383-387, (1998).

Hubbel, J. H., Wm. J. Veigele, E. A. Briggs, R. T. Brown, D. T. Cromer and R. J. Howerton. "Atomic Form Factors, Incoherent Scattering Functions, and Photon Scattering Cross Sections". J. Phys. Chem. Ref. Data. Vol. 4, No. 3, (1975).

Leunbach, I. "Three Dimensional Imaging and Tomography Using Compton Scatter". IAEA: Medical Radionuclide Imaging. Vol. 1, 263, (1997).

Martin, Jeffrey B. Personal Interview. 1998.

McClean, B.A., T.R. Overton, T.N. Hangartner and S. Rathee. "A Special Purpose X-Ray Fan-Beam CT Scanner for Trabecular Bone Density Measurement in the Appendicular Skeleton". Phys. Med. Biol. Vol. 35, No. 1, 11-19 (1990).

Newman D L, Dougherty G, Al Obaid A, and Al Hajrasy, H. "Limitations of clinical CT in assessing cortical thickness and density". Phys. Med. Biol. Vol. 43, 619-626, (1998).

Ordonez, Caesar E., Alexander Bolodynya, and Wei Chang. "Doppler Broadening and Energy Uncertainties in Compton Cameras." IEEE Nuclear Science Symposium and Medical Imaging Conference. Conference Record, (1997).

Plein & Baus, GmbH, Multi – The Data Acquisition Program for IBM-PC/CAMAC Based Multi Parameter Experiments (software manual), April 1993.

Plein & Baus, GmbH, Camac Crate Controller CC16 User Manual, November 1994.

Lunar, DPX Operators Manual, 1993.

Lunar, DPX Technical Manual, 1993.

Narhi, Diane. Osteoporosis Center of Simmi Valley. http://www.osteoexam.com/osteoporosis.html. 21 September 1998.

National Osteoprosis Foundation. http://www.nof.org. 21 September 1998.

Norton, Stephen J. "Compton Scattering Tomography". Journal of Applied Physics Vol. 76, No. 4, (1997).

Prettyman, T.H., R.P. Gardner, J.C. Russ and K. Verghese. "A Combined Transmission and Scattering Tomographic Approach to Composition and Density Imaging". Appl. Radiat. Isot. Vol. 44, No.10/11, 1327-1341, (1993).

Ruegsegger, Peter, Max Anliker and Maximilian Dambacher. "Quantification of Trabecular Bone with Low Dose Computed Tomography". Journal of Computer Assisted Tomography. Vol. 5, No. 3, 384-390, (1981).

Tortora, Gerard J., and Nicholas P. Anagnostakos. Principles of Anamoty and Physiology. 5th Edition. Harper & Row, New York, NY. pp.120, 1987.

Vorob'ev, V. A. and V. A. Gorshkova. "Reconstructive Tomography in Back-Scattered Radiation". Russian Journal of Nondestructive Testing. Vol. 32, No. 3, (1996).

Webber, C.E., and T.J. Kennett. "Bone Density Measured by Photon Scattering". Phys. Med. Biol., Vol. 21, No. 5, 760-769, (1976).

VITA

Captain Marc J. Sands was born on 18 June 1972 in San Diego, California [Birth Certificate #09740, Local District #8009]. In 1990 he graduated from St. Patrick-St. Vincent High School in Vallejo, California. He entered undergraduate studies at the United States Air Force Academy in Colorado Springs, Colorado, and graduated in June 1994. He received his Air Force commission on 01 June 1994. His first assignment was to the Headquarters, National Air Intelligence Center at Wright-Patterson Air Force Base, Dayton, Ohio where he worked as analyst and system developer of a research and development space surveillance system. In August 1997, he entered the School of Engineering, Air Force Institute of Technology.

Captain Sands is married to the former Angela H. Sturm, of Delaware, Ohio who is currently a 1st Lieutenant in the U.S. Air Force Nurse Corps at Wright-Patterson Air Force Base.

REPORT DOCUMENTATION PAGE

1. AGENCY USE ONLY *(Leave blank)*	2. REPORT DATE 08 March 1999	3. REPORT TYPE AND DATES COVERED Final

4. TITLE AND SUBTITLE
An Investigation Into the Noninvasive Assessment of Bone Density Using Multiplexed Compton Scattered Tomography

5. FUNDING NUMBERS

6. AUTHOR(S)

Marc J. Sands, Captain, USAF

7. PERFORMING ORGANIZATION NAME(S) AND ADDRESS(ES)
AFIT/ENP
Advisor: Jeffrey B. Martin, Major, USAF; Comm (937) 255-3636
2950 P. Street
Wright-Patterson AFB, OH 45433

8. PERFORMING ORGANIZATION REPORT NUMBER

AFIT/GAP/ENP/99M-10

9. SPONSORING/MONITORING AGENCY NAME(S) AND ADDRESS(ES)
74th Medical Group (SGSXT)
Attention: William R. Ruck, II, Major, USAF; Comm (937)257-0455
4881 Sugar Maple Drive
Wright-Patterson AFB, OH 45433

10. SPONSORING/MONITORING AGENCY REPORT NUMBER

11. SUPPLEMENTARY NOTES

12a. DISTRIBUTION AVAILABILITY STATEMENT

Approved for public release; Distribution unlimited

12b. DISTRIBUTION CODE

13. ABSTRACT *(Maximum 200 words)*

The purpose of this research is to investigate the application of a Compton scatter imaging technique to measure bone density. A demonstration Multiplexed Compton Scatter Tomograph (MCST) was assembled to demonstrate the feasibility of detecting osteoporosis by modifying a system originally designed to detect hidden corrosion in aluminum aircraft wings. Measurements were performed on an aluminum phantom representing a wrist bone containing varying densities in the center and varying thickness of the cortical shell. The densities in the center are comparable to normal trabecular bone, sixty-percent of normal trabecular bone and a void. The MCST images of the phantom were then compared to simulated images from a detector. The images and simulations were also compared to images from a clinical computed tomography (CT) scanner. Based on the results, the MCST can discern the features represented by the trabecular bone. The system was able to differentiate normal, osteoporotic and void densities.

14. SUBJECT TERMS
Compton scatter, Compton scatter tomography, trabecular bone, trabecular density measurements, bone density measurements, osteoporosis, osteoporosis detection, hololo

15. NUMBER OF PAGES
83

16. PRICE CODE

17. SECURITY CLASSIFICATION OF REPORT	18. SECURITY CLASSIFICATION OF THIS PAGE	19. SECURITY CLASSIFICATION OF ABSTRACT	20. LIMITATION OF ABSTRACT
Unclassified	Unclassified	Unclassified	UL